

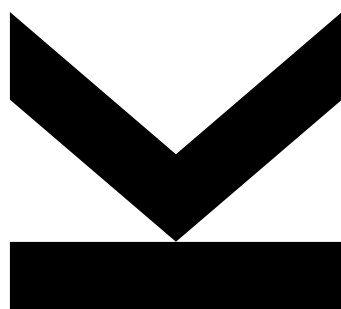
Author
Katarina Gugujonović
BSc

Submission
**Institute of Physical
Chemistry and
Linz Institute of
Organic Solar Cells**

Thesis Supervisor
Assoc. Prof.
DI Dr. Markus Scharber

July 2020
(revised September 2020)

PHOTOLUMINESCENCE ENHANCEMENT IN PEROVSKITE THIN FILMS



Master's Thesis

to confer the academic degree of

Master of Science

in the Master's Program

Chemistry and Chemical Technology

Acknowledgement

My biggest thanks go to my supervisor Assoc. Prof. DI Dr. Markus Scharber who invested so much time in discussions concerning my work and who provided me with all the required facility. Thanks for your guidance, encouragement and support, but also for leaving me space to realise my own ideas in my work.

I would like to thank o.Univ. Prof. Mag. Dr. DDr. H.c. Niyazi Serdar Sariçiftçi for giving me the opportunity to work on this special topic and together with his fantastic team.

I would like to express my special thanks to my good friend Felix Mayr, BSc. for the time he invested for talk shop, for the in-depth discussions and for his great emotional support.

Also big thanks to Lukas Lehner, BSc., Dr. Bekele Teklemariam Hailegnaw and Jakob Hofinger, MSc. for the scientific talks we had so many times and for helping me with interpretation of new insights during my work.

Big thanks to Christoph Putz, BSc. for helping me handling problems with LaTeX. Without you I would not have been able to realize my thesis in this format.

Thank you Dominik Wielend, MSc. for the enjoyable conversations, being my personal reminder and for your administrative assistance.

Big thanks to Patrick John Denk and Dr. Munise Cobet for their kind support and for helping me with technical issues.

I would like to express my special thanks to my good friend Anna Reitingner for your support and of course for your time and effort while proofreading this thesis.

I would also like to extend my gratitude to my parents and my friends for bolstering me. Especially I would like to thank Manuel Schullitsch who can easily break my inner barriers and for being a brilliant motivator.

Thanks to the whole LIOS group with whom I collected so many remarkable memories during work and also during celebrations. I am very pleased to be part of this fantastic international team who has members all around the world. Everyone loves to help when you have specific questions and that is a rarely found characteristic which should not be taken for granted.

Abstract

Organic-inorganic hybrid perovskites are a material class that are already highly investigated for third generation photovoltaics, light emitting diodes, photodetectors etc. Due to their outstanding properties they are promising candidates for highly efficient energy conversion. Nevertheless there is still room for further gains in terms of loss reduction and consequently improvement of the overall performance of the device. A high luminescence quantum yield is a prerequisite for semiconductors used for this applications. In this thesis several possibilities of luminescence improvement are discussed. The focus is on materials that can passivate the perovskite layer from the surface and eliminate dangling bonds and other trap states by engineering of the band structure. Besides, also components that can be intercalated into the perovskite layer and reduce non-radiative recombination centers are examined. The reduction of non-radiative recombination centers leads to an enhancement of the luminescence. Correspondingly, the open circuit potential is increased which is an important characteristic of the final photovoltaic device.

Kurzfassung

Organisch-anorganische hybrid Perowskite sind eine bereits weitgehend erforschte Materialklasse für Photovoltaik Materialien der dritten Generation, LED-Leuchtmittel, Photodetektoren uvm. Aufgrund ihrer überragenden Eigenschaften sind sie vielversprechende Materialien für hocheffiziente Energieumwandlung. Die Herausforderung zur Optimierung der Gesamteffizienz dieser Bauteile durch Eindämmung der Verluste bleibt jedoch immer noch bestehen. Eine Voraussetzung für die hierfür verwendeten Halbleitermaterialien ist eine hohe Lumineszenz-Quantenausbeute. In dieser Arbeit werden verschiedene Methoden zur Erhöhung und Optimierung der Lumineszenz diskutiert. Der Fokus liegt auf Materialien, die als Oberflächenpassivierungsmittel dienen und Rekombinationszentren durch Modifizierung der Bandstruktur eliminieren können. Daneben werden auch Additive, welche durch Interkalation in das Perowskitgitter eingebettet werden und dadurch weitere nicht-strahlende Rekombinationszentren passivieren, untersucht. Die Verminderung der nicht-strahlenden Rekombinationszentren führt zu einer Erhöhung der Lumineszenz. Dementsprechend liegt eine Erhöhung der Leerlaufspannung vor, wodurch eine wichtige Eigenschaft zur Verbesserung der Bauteileffizienz verbessert werden kann.

Contents

1	Introduction	7
1.1	Luminescence quantum yield	8
1.2	Suppression of non-radiative recombination	10
1.2.1	Passivation by coordinate bonding	13
1.2.2	Passivation by ionic bonding	14
1.2.3	Passivation by conversion to layered heterostructures	15
2	Experimental	18
2.1	Materials	18
2.1.1	Perovskites as photoactive materials	19
2.1.2	PEDOT:PSS, Zonyl FS-300	20
2.1.3	Synthesis of methylammonium iodide	21
2.2	Thin film fabrication	21
2.2.1	General processing	21
2.2.2	Anti solvent technique	23
2.2.3	Preparation of methylammonium lead iodide thin films with trioctyl-phosphine oxide passivation	23
2.2.4	Investigation of methylammonium lead iodide interaction with trioctyl-phosphine oxide	24
2.2.5	Preparation of methylammonium lead iodide thin films with water additive	24
2.2.6	Preparation of methylammonium lead iodide thin films with slight excess of a precursor component	24
2.2.7	Preparation of methylammonium lead iodide thin films with lead chloride additive	25
2.2.8	Preparation of methylammonium lead iodide thin films with benzylamine passivation	25
2.2.9	Preparation of methylammonium lead iodide thin films with tetrabutyl-ammonium iodide additive	25
2.2.10	Preparation of methylammonium lead iodide thin films with tetrahexyl-ammonium iodide and tetrabutylammonium iodide additive (combinatory method)	26
2.2.11	Preparation of methylammonium lead iodide thin films with tetrapropyl-ammonium iodide	26
2.3	Solar cell fabrication	26
2.4	Photoluminescence	27
2.5	IV-characterization	27

2.6	UV-VIS spectroscopy	27
2.7	Scanning electron microscopy	27
3	Results and discussion	28
3.1	Coordinate bonding	28
3.1.1	Influence of trioctylphosphine oxide	28
3.1.2	Influence of water	29
3.2	Ionic bonding	31
3.2.1	Influence of lead iodide and methylammonium iodide in slight excess	32
3.2.2	Influence of lead chloride and comparison of recipes	32
3.3	Conversion to layered structures	34
3.3.1	Influence of benzylamine	34
3.3.2	Influence of tetrabutylammonium iodide	35
3.3.3	Influence of tetrabutylammonium iodide and tetrahexylammo- nium iodide combinations	37
3.4	Implementation of an additive into a solar cell	38
4	Conclusion and outlook	40

1 Introduction

Lead halide perovskites, especially hybrid organic-inorganic halide perovskites (OIHP), have attracted huge attention in the last decades. Due to their outstanding properties, like strong ability to absorb light of the visible spectra [1, 2], long carrier diffusion length [2, 3], high charge mobility [4] and tunable band gap [5] they are promising candidates for many opto-electronic applications like solar cells [1, 6–9] and light emitting diodes [10–14]. OIHP thin films can be processed directly from their precursor solution, which makes manufacturing of the devices easy and fast. The most prominent OIHP materials that are used as photoactive layers in solar cells are based on polycrystalline methylammonium lead iodide (MAPI). To facilitate efficient charge transport, dense films with nearly no vacancies, which could function as recombination centers, are essential. Electrons and hole can recombine radiatively and non-radiatively, depending on the energy set free in this reaction. Radiative recombination is a mechanism where photons are created, whereas non-radiative recombination leads to the formation of phonons [15]. The probability of radiative recombination increases by sealing the non-radiative recombination centers. It has been shown that the number of emitted photons, or in other words, the luminescence of a photoactive material makes an essential contribution to the performance of a photovoltaic device [16]. As a consequence, the production of efficient photovoltaic devices is challenged by the formation of dense and uniform absorber materials. This can be achieved with optimized process parameters and conditions during the manufacturing [17]. With anti solvent treatment, where an immiscible solvent is added during spin coating, an improvement of the surface morphology can be achieved. Commonly used anti solvents are chlorobenzene [18, 19], toluene [19], methoxybenzene [20] and ethylacetate [21]. As an alternative, drop casting of the anti solvent [22] or solvent vapour annealing with the solvent that was used for the precursor solution, usually dimethylformamid (DMF) [23], can be done to achieve uniform films. Additives that can migrate to the vacancies and passivate the grain boundaries can be blended directly into the precursor solution or applied on top of the perovskite film. That is the reason why many variations of MAPI are known nowadays, for example materials with triple cation [24] combinations and mixed halide perovskites [5, 25]. These blends show enhanced stability and increased efficiency of the device. The performance and stability of the device can be improved by surface and interface engineering, since surfaces are critical for the exciton formation, charge carrier extraction, exciton recombination and the degradation of the photoactive film in the device [26]. Layers like trioctylphosphine oxide (TOPO) [1, 27, 28], alkylamines [29] and Polyphosphazene [30] can be processed on top of the peroxide layer to

passivate the surface of the film. Another method of improving the perovskite film formation is solvent engineering, where a miscible solvent is added to the precursor solution. These additional compounds contain specific groups that can coordinate with the lead(II) atom. The formed intermediate influences the crystallization and the kinetics of the perovskite growth, which has an immense impact on the grain size, the morphology and the coverage of the film [25, 31, 32]. DMSO is one example that can form such kind of intermediate by coordination of two DMSO molecules via their oxygen atoms to lead(II) iodide [22, 32, 33]. A similar phenomenon occurs by using less polar acetylaceton instead of DMSO. Here, the lead(II) ion is chelated by two acetylaceton ions to form a complex [25, 31, 34].

1.1 Luminescence quantum yield

OIHPs can exhibit a sharp photoluminescence signal, which indicates fast relaxation and recombination [35]. The understanding of the physical processes going on in the semiconductor is necessary for improving an OIHP device. The concept of chemical potential of light describes the interaction of photons with matter. Photons can be generated or taken up by the excitation of electrons from the valence band to the conduction band. As a consequence, an electron-hole pair is generated and a so-called exciton is formed. If the electrons and holes are not extracted from the electrodes, recombination is very likely and a photon is formed again. Fig. 1 illustrates this process schematically. In this process the photon momentum and the angular momentum are conserved, whereas the number of particles in the matter is not conserved. The temperature and the chemical potential of photons are deduced from these interactions. Distinction between thermal and non-thermal radiation is necessary. Thermal radiation is generated by black body radiators and can be described according to Planck's law. If the black body radiator is in thermal equilibrium with the semiconductor, the chemical potential is zero. The emitted light of a thermal radiator is broad and relatively low compared to a non-thermal radiator, because the signal is only a function of the temperature. The signal of a non-thermal radiator is indicated by its remarkably high intensity. The predominant energy states that are involved in the interaction between photon and matter are shown in the same figure. The electrical potential energy for electrons gives the change in free energy, resulting from adding or removing electrons from the system. It is defined as the product of the electrical potential ϕ and the charge of the electron e . The chemical potential μ_e of electrons corresponds to the sum of the chemical potential for the undoped matter $\mu_{e,0}$ and a term that represents the p-doping concentration $kT \ln \frac{n_e}{N_C}$. The chemical potential of holes can be defined similarly to that of electrons.

1.1 Luminescence quantum yield

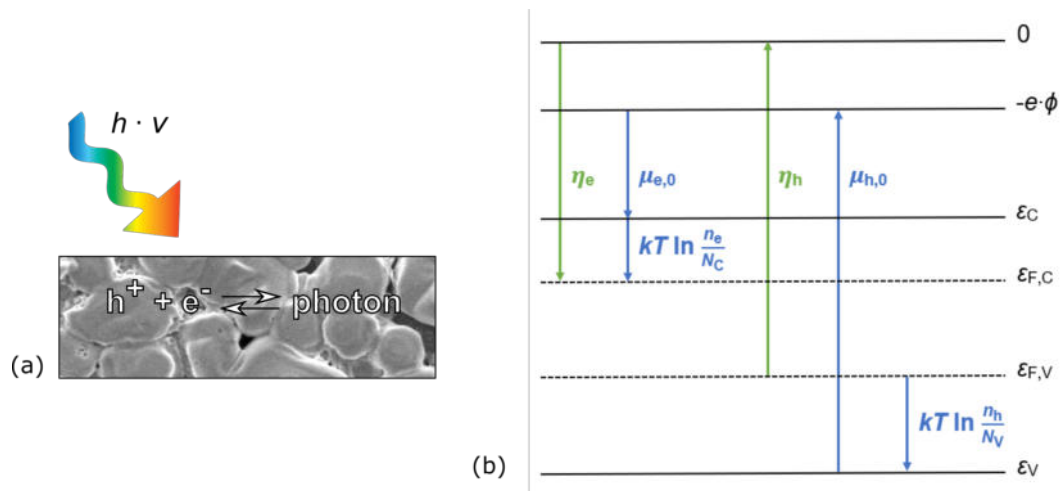


Figure 1: (a) Schematic illustration of electron-hole-pair generation via light absorption and reversible reaction for photon generation. (b) Energy diagram for the involved energy states in the absorption process of a photon. η_e ... electrochemical potential of electrons, $\mu_{e,0}$... chemical potential of electrons, $\frac{n_e}{N_C}$... n-doping concentration, η_h ... electrochemical potential of holes, $\mu_{h,0}$... chemical potential of holes, $\frac{n_h}{N_V}$... p-doping concentration

By considering the electrical potential, the electrochemical potential of electrons η_e can be derived. By assuming thermal equilibrium, the electrochemical potential of electrons can be identified as their Fermi energy ϵ_{FC} as written in Eq. 1 [15, 16, 36, 37].

$$\eta_e = \epsilon_{FC} , \quad (1)$$

The electrochemical potential of holes is given by Eq. 2.

$$\eta_h = -\epsilon_{FV} , \quad (2)$$

The Fermi energy is usually centered between the valence band and the conduction band. When electrons are excited by the absorption of light, the quasi-Fermi level of the conduction band increases and the quasi-Fermi level of the valence band drops below the equilibrium Fermi level. The sum of the chemical potentials is the difference of the quasi-Fermi energies of the electrons in the conduction band and holes in the valence band. The chemical energy per electron-hole pair represents the maximum produced energy when illuminating a semiconducting absorber and is therefore equal to V_{OC} . The more light is shining on the system the higher the

quasi-Fermi level splitting [15, 16].

$$\mu_e + \mu_h = \varepsilon_{FC} - \varepsilon_{FV} = V_{OC} , \quad (3)$$

As described in the work from Shockley and Queisser, a good solar cell is also a good radiative emitter [38]. The ratio of the emitted photons to the photons absorbed gives the photoluminescence quantum yield η_{ext} , which is an attractive characterization tool to describe the quality of absorber materials. The correlation between V_{OC} and η_{ext} is given in Eq. 4. $V_{OC, rad}$ is defined as the open circuit voltage when only radiative recombination occurs, k is the Boltzmann constant and T the temperature in K. The more light is emitted after photoexcitation, the higher the open circuit voltage. The highest V_{OC} would be achieved with a quantum efficiency near 1. In this case all generated excitons need to recombine radiatively [16, 39].

$$V_{OC} = V_{OC, rad} + \frac{kT}{q} \cdot \ln(\eta_{ext}) , \quad (4)$$

1.2 Suppression of non-radiative recombination

Although OIHP thin films show good properties for solar cell applications, losses exist that need to be suppressed to achieve maximum performance [15, 30, 39–41]. Beside optical and ohmic losses, the most dominant losses arise from recombination. Charge carriers which are generated in the photoactive layer and are not collected at one of the electrodes are lost by recombination [15]. Especially for thin film photovoltaics, the elimination of recombination centers at the interfaces, as well as in the bulk is essential [30, 42]. In most cases recombination centers in the bulk are induced through impurities. Recombination centers at the surface are very likely at the contacts, due to increased defect density [40]. The challenge in manufacturing high performing photovoltaic devices is to reduce recombination centers at the surface of the material, as well as in the bulk.

Charge carriers can recombine radiatively or non-radiatively by generating photons or a number of phonons, respectively. The possible recombination mechanisms are listed in Fig. 2. The most obvious recombination mechanism is the radiative recombination where an electron from the conduction band reacts with a hole and forms a photon. It is exactly the reverse reaction of the absorption process. Since an electron and a hole need to meet each other for recombining, the recombination rate R_{rad} is a function of their concentration in the bulk n_e and n_h , respectively. The

1.2 Suppression of non-radiative recombination

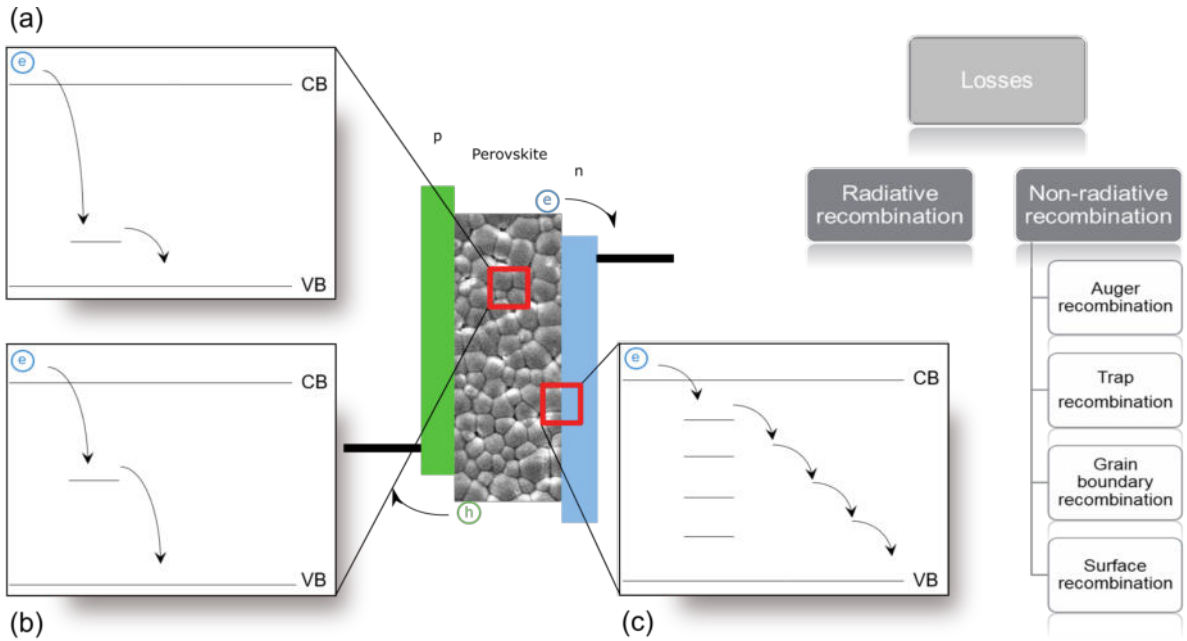


Figure 2: Schematic illustration of recombination mechanism in a p-i-n perovskite solar cell. (a) Recombination via shallow level traps. (b) Recombination via deep level traps. (c) Recombination via surface states continuously distributed over the energy gap.

correlation is shown in Eq. 5. B is the coefficient for radiative recombination for a specific material. For silicon this factor is found to be $3 \times 10^{-15} \frac{\text{cm}^3}{\text{s}}$ [15]. For MAPbI₃ the radiative recombination coefficient is between $0.6 \times 10^{-10} - 1.1 \times 10^{-10} \frac{\text{cm}^3}{\text{s}}$ [43], which is comparable with classical III-V semiconductors with direct band gaps [15, 39, 40].

$$R_{\text{rad}} = B \cdot n_e \cdot n_h, \quad (5)$$

The smaller the energy between the essential states, the lower the number of phonons generated and the more likely is the process of non-radiative recombination. Auger recombination is a non-radiative recombination process where three particles are involved. Here, the energy set free from the recombination process between an electron and a hole is taken up by a third charge carrier (either an electron or a hole). The excess energy of the third particle is then lost through collision with phonons from the lattice. The probability of Auger recombination is correlated to the doping level of the material and to the charge carrier mobility. The recombination rate $R_{\text{Aug, e}}$ for Auger recombination in an n-doped semiconductor is given by Eq. 6. It is higher the stronger the n-doping [15, 40, 44].

1.2 Suppression of non-radiative recombination

$$R_{\text{Aug, e}} = C \cdot n_e^2 \cdot n_h , \quad (6)$$

The recombination rate in a p-doped material increases analogue by increasing the doping concentration, as shown in Eq. 7.

$$R_{\text{Aug, h}} = C \cdot n_h^2 \cdot n_e , \quad (7)$$

The probability of Auger recombination in MAPI is relatively low due to the low charge carrier density as it is not doped and the low charge carrier mobility of $2 \text{ cm}^2\text{s}^{-1}\text{V}^{-1}$ [4]. The predominant recombination process is the recombination via impurities which is also known as Shockley-Read-Hall recombination [45]. Some contaminations can introduce energy levels in the band gap. Energy levels that are located in the middle of the band gap are called deep level traps. An illustration is shown in Fig. 2 (a). If the additional energy levels are either near the valence band or the conduction band, one is talking about shallow energy traps (Fig. 2 (b)). Deep level traps are critical centers for non-radiative recombination, because in case of shallow energy traps the charge carriers can be re-emitted into the band it came from by absorption of phonons. An electron moving through the lattice has a thermal velocity ν_e . σ_e is the capture cross section of this electron for an impurity center that is occupied by a hole. The impurity recombination rate $R_{\text{imp, e}}$ is proportional to both of these parameters, as shown in Eq. 8 and analogue for a hole in Eq. 9. $n_{\text{imp, h}}$ is the density of impurity states occupied by a hole [15, 39, 40].

$$R_{\text{imp, e}} = \sigma_e \cdot \nu_e \cdot n_e \cdot n_{\text{imp, h}} , \quad (8)$$

$$R_{\text{imp, h}} = \sigma_h \cdot \nu_h \cdot n_h \cdot n_{\text{imp, e}} , \quad (9)$$

For atoms that are located at the surface of a semiconductor, one or more binding partners are missing. In this case the surface is covered by so-called dangling bonds which can easily absorb impurities like water or oxygen. Surface trap states are continuously distributed over energy in the band gap as shown in Fig. 2 (c). For solution-processed polycrystalline perovskite films, the surface area is increased compared to the surface area in single crystals due to the presence of grain boundaries. Therefore not only elimination of trap centers in the bulk, but also passivation

of the surface is an essential point in the production of high-quality perovskite thin films [1, 7, 15, 40, 46, 47]. The recombination rate $R_{s,e}$ is defined similarly to the impurity recombination process for electrons (Eq. 10) and holes (Eq. 11). $n_{s,e}$ and $n_{s,h}$ are the density of surface states occupied by a hole or an electron, respectively. [15, 40].

$$R_{s,e} = \sigma_{s,e} \cdot \nu_e \cdot n_e \cdot n_{s,h} , \quad (10)$$

$$R_{s,h} = \sigma_{s,h} \cdot \nu_h \cdot n_h \cdot n_{s,e} , \quad (11)$$

The challenge is to improve the photoluminescence quantum yield by sealing the non-radiative recombination centers. This can be achieved by using either additives for the precursor solution or directly applying a passivating layer on top of the perovskite thin film. Possible passivation techniques will be discussed in the next chapter.

1.2.1 Passivation by coordinate bonding

For the passivation via coordinate bonding, a Lewis acid and a Lewis base get together to form a Lewis adduct. For this either a Lewis acid or a Lewis base can be used as additive since defects in the crystal can have both characteristics. Lewis acids can passivate electron rich defects which are a consequence of undercoordinated I⁻ and antisite PbI_3^- . These defects contribute to the formation of deep energy traps at the surface and at the grain boundaries [46]. Popular acceptor materials are fullerenes which were first used by the group of Sariciftci et al. for photovoltaic applications [48]. A common derivative, which is also used as electron transport layer in perovskite solar cells, is Phenyl-C61-butyricacidmethylester (PC_{60}BM). The additional side chain increases the solubility of the material in aromatic solvents which enables the usage of simple manufacturing techniques [49]. PC_{60}BM smoothes the surface and enables sufficient electron transfer [50]. It was shown that the use of PC_{60}BM can reduce trap density and reduce hysteresis effects in perovskite solar cells [51, 52]. It reacts with halide rich defects by altering its shape while accepting an electron and therefore reducing the intrinsic strain [39, 53, 54]. In contrast, Lewis bases can react with undercoordinated Pb^{2+} or Pb clusters to form an adduct. Typical additives have functionalities with one or more lone pairs and contain heteroatoms like phosphor, oxygen, sulfur or nitrogen [46, 55]. A material investigated in this thesis is trioctylphosphine oxide (TOPO), which is commonly known as an extractant

for metal ions [56, 57]. Here, the electronegative oxygen can bond to defects in the lattice and passivate them [46, 58]. Braly et al. reported a significant increase of the photoluminescence quantum yield as well as an enhancement of the quasi-Fermi level splitting by using TOPO as passivation agent. They could achieve an internal quantum yield approaching unity under 1 sun [1]. Also, moisture and oxygen have a substantial influence on perovskites. To a certain extent, they can improve the performance by spontaneous passivation [59, 60]. Since water has ambivalent characteristics it can function as Lewis base via O coordination or as Lewis acid via coordination through hydrogen bonding. Yu et al. reported an improvement of the layer formation when adding protons to a methylammonium lead bromide solution in form of HBr. The additive increased the solubility of the precursor components in the solvent and delayed the crystal formation rate [10]. It is also known, that MAPI devices are particularly sensitive on water, since it probably is part of the decomposition pathway [26]. Therefore, water can also have negative effects on the performance of the device. Due to difficulties of generating completely oxygen and moisture free conditions, the impact on OIHs is not fully understood and needs further investigations.

1.2.2 Passivation by ionic bonding

The passivation via ionic bonding is possible because of the charged nature of defects of OIHs. It includes the complete transfer of one or more valence electrons and leads to a strong electrostatic interaction between two ions [39]. Cations can passivate negatively charged defects like undercoordinated I⁻, antisite PbI₃⁻ and methylammonium (MA⁺) vacancies. Promising candidates are for example metal ions like Na⁺ [61], K⁺ [62], ammonium [63, 64], Cs⁺ [24, 65, 66], Eu⁺ [67] or organic cations like formadinium [24, 66, 68], phenethylammonium [47, 68], benzylammonium [69] or alkylammonium derivatives [7, 29]. Therefore, often combinations of more than one cation eg. triple-cation compounds are used for OIHs. Small cations can diffuse through grain boundaries and eliminate the non-radiative recombination states caused by dangling bonds [61]. In case of organic molecules the size plays an important role. A too large molecule can form lower dimensional perovskite [7, 70–72]. The conversion into layered structures will be discussed in 1.2.3. Anions can passivate undercoordinated Pb²⁺ ions and halide vacancies [39]. A popular agent is chlorine which can be added in various different forms like PbCl₂ [7, 73], NH₄Cl [66, 74], methylammonium chloride [75], formadinium chloride [76] or cesium chloride [77]. It is known that most of chlorine leaves the film during the annealing process [78]. And still, some chlorine atoms can be found in the film, suggesting that the remaining atoms are embedded in the lattice defects and ensure a passivating effect

[73, 79]. The implementation of chlorine leads to a change of the electronic properties of the film and to the formation of larger grains [46, 73]. The impact is reflected in the enhanced lifetime of chlorine doped devices [39, 75]. Slight excess of one of the precursor components also acts as passivation agent through ionic bonding. For example, an excess of lead iodide can reduce the trap concentration caused by halide vacancies and favour the formation of uniform crystals [8]. An excess of MAI leads to segregation of this material from the crystal. As a consequence a thin MAI coating is achieved, which passivates each particular grain [80]. Another possibility to passivate positively charged vacancies is the use of carboxylate groups. Here, it strongly depends on the pK_a value if the deprotonated species is either bound via ionic bonding or, in case of the hydrogenated group, via hydrogen bonding [81, 82]. Also thiocyanate doping can be used for passivation. It similarly affects the perovskite thin film like it affects chlorine by increasing the grain size and can bond to undercoordinated lead [63, 64, 83].

1.2.3 Passivation by conversion to layered heterostructures

Conversion of dangling bonds as passivation technique is already highly investigated for silicon, where the surface of the material can be converted into SiN_x or SiO_2 [84–89]. The conversion of a perovskite surface to a wide band gap semiconductor eliminates the trap states at the surface, as well as at the grain boundaries. Beside that, a type-I band alignment is formed to further suppress non-radiative recombination [46]. Perovskites can be processed into lower dimensional semiconductors including zero-dimensional (0D), one-dimensional (1D) and two-dimensional (2D) structures [90]. Exceedingly high fluorescence can arise from quantum dot systems. Their spatial confinement leads to the formation of discrete quantum states. Their optical and physical properties resemble these of bulk semiconductors, as well as of single molecules [91]. In quantum wire systems, charges can only move in one spatial direction. In case of two-dimensional structures one is talking about quantum-well systems. As shown in Fig. 3, a larger A cation is intercalated between the octahedrons to form a lower dimensional (layered) perovskite structure [39, 90]. The large organic cation might be pushed towards the edge of a grain and form a passivating layer, which means that the two dimensional structure is located at the surface of the semiconductor [7, 68, 92]. By increasing the number of bulky cation layers, the band gap increases too [90]. The lower edge of the conduction band is lifted and the upper edge of the valence band is lowered upon conversion [39, 68]. Therefore the dangling bonds on the surface are eliminated and a thin passivating layer is formed [69, 92]. However, large organic molecules are electrical insulators and charges can be blocked to a certain degree when implementing them into the semiconductor bulk.

1.2 *Suppression of non-radiative recombination*

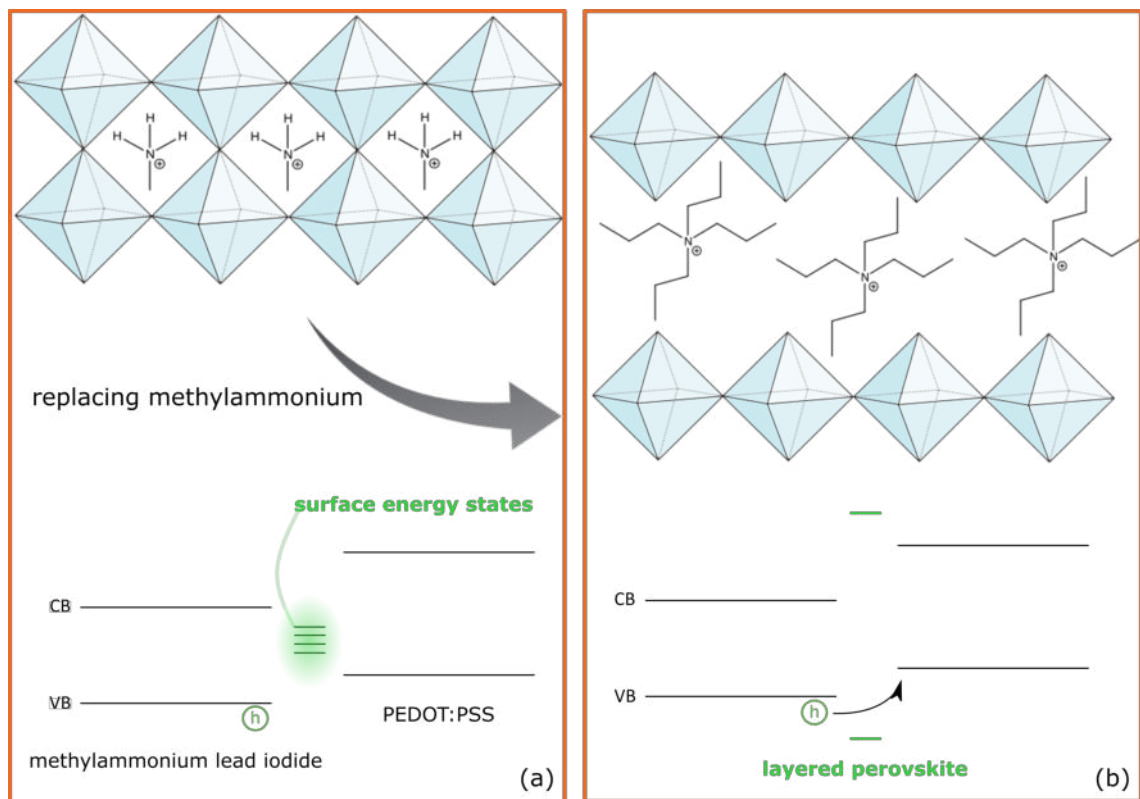


Figure 3: (a) Simple methylammonium lead iodide structure and energy diagram with illustrative dangling bonds between the perovskite-PEDOT:PSS-interface. (b) Two-dimensional perovskite with intercalated tetrabutylammonium molecules between the octahedra and energy diagram with type-I alignment via conversion of pristine perovskite structure to wide band gap semiconductors.

For solar application a balance must be found between elimination of non-radiative recombination zones and presence of insulating material that hinders the charge transport to the electrodes. Different techniques are currently being studied, where a vertical arrangement of the bulky A cations is tried to be obtained [92]. The formation of heterostructures leads to a higher stability of the entire device [7].

“God made the bulk, the surface was invented by the devil.” - Pauli

2 Experimental

2.1 Materials

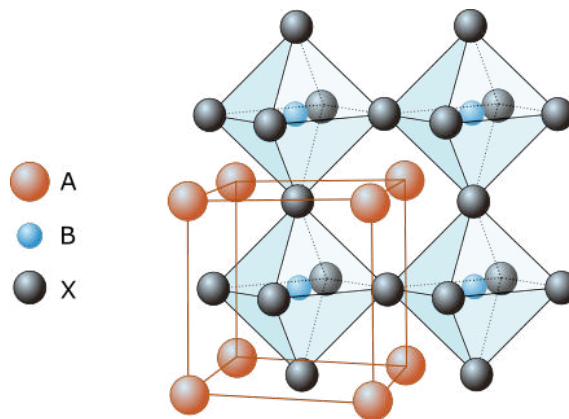
Table 1: Overview of used materials, including supplier, purity and abbreviation.

Material	Supplier	Purity / %	Abbr.
Acetylacetone	Sigma Aldrich	≥ 99	AA
Aluminum	chemPUR	99.999	Al
Ammoniak	Donauchem	24.5	-
Benzylamine	Sigma Aldrich	99	BA
Chlorobenzene	Alfa Aesar	99.8	CB
Diethylether	VWR chemicals	100.0	-
Dimethylsulfoxide	VWR chemicals	99.7	DMSO
Hydrochloric acid	VWR chemicals	37	HCl
Hydrogen Peroxide	Merck	30	-
Hydroiodic acid	Merck	57	HI
Indium doped tin oxide on glass	Xinyan Hongkong	-	ITO
Lead(II) acetate trihydrate	Aeros Organics	99.999	Pb(OAc) ₂
Lead(II) chloride	Alfa Aesar	99.999	-
Lead(II) iodide	Alfa Aesar	99.9985	-
Methylamine	Sigma Aldrich	33	MA
Methylammonium iodide	-	-	MAI
N,N-Dimethylformamide	Sigma Aldrich	99.8	DMF
Phenyl-C61-butyracacidmethylester	Solenne	99	PC ₆₀ BM
Poly(3,4-ethylenedioxy-thiophene):poly(styrene-sulfonate) (Clevios PH 1000)	Heraeus	-	PEDOT:PSS
2-propanol	Merck	100.0	IPA
Tetrabutylammonium iodide	Alfa Aesar	98	TBAI
Tetrahexylammonium iodide	Fluka	99	THAI

Table 2: Overview of used materials, including supplier, purity and abbreviation.

Material	Supplier	Purity / %	Abbr.
Tetrapropylammonium iodide	Sigma Aldrich	98	TPAI
Trioctylphosphine oxide	Fluka	98.5	TOPO
Zonyl FS-300 Fluorinated Surfactant	abcr	-	-

2.1.1 Perovskites as photoactive materials

**Figure 4:** Perovskite structure in ABX_3 configuration.

Perovskite originally refers to a ceramic material class which naturally occurs in the calcium titanate structure (CaTiO_3) in the configuration ABX_3 . Gustav Rose was the first who discovered this material class in 1839. He named it "Perowskit" (germ.) or "perovskite" (engl.) in honor of the russian vice president and mineralogist Lew Alexejewitsch Perowski [93]. The atoms that can form a perovskite structure need to have a certain proportional ratio, which can be described with the Goldschmidt tolerance factor α as given in Eq. 12. r_A , r_B , and r_X are the radii of the atoms A, B and X, respectively. The coefficient α is a factor between 0.8 and 1.0 [94]. B is surrounded by an octahedron of X atoms and A is located between the octahedra. In case of $\alpha = 1$, a perfect octahedron is formed. A schematic illustration of the cubic unit cell is shown in Fig. 4.

$$\alpha = \frac{r_A + r_X}{\sqrt{2} \cdot (r_B + r_X)}, \quad (12)$$

OIHPs can undergo a phase transition between orthorhombic to tetragonal and tetragonal to cubic, respectively [46, 95]. The phase transition can be stimulated with

temperature [46, 96], pressure [97, 98] and applying a magnetic [99, 100] or electric field [101, 102]. The effect is reflected in a changed opto-electronic character of the perovskite structure. In OIHPs, the A atom is replaced by an organic cation, B is replaced by a metal cation and X is a halogen anion [2, 103, 104]. In case of MAPI, the atom A is a methylammonium cation, B is lead and X is iodide. This composition gives a broad absorption spectra for visible light with a band gap between 1.5 - 1.6 eV [96]. Due to steric constraints of the constituents (in case of $\alpha < 1$), the structure is slightly distorted [2]. Although perovskite as material class is known for quite some time, the use as absorber material in solar cells is relatively recent. The history of these materials is short but explosive. The first OIHP solar cell was reported by Miyasaka et al. [105] in 2009. They achieved a maximum efficiency of 3.81%. Since then the research in perovskite materials as visible light absorbers drastically increased. Today the highest reported efficiency is 25.2% [106].

2.1.2 PEDOT:PSS, Zonyl FS-300

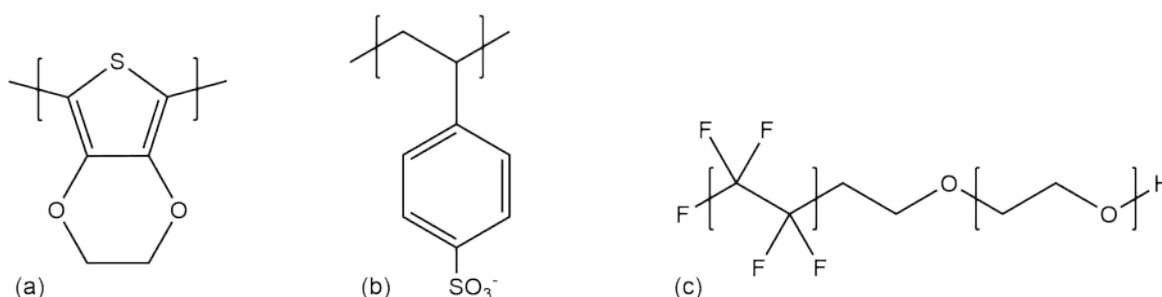


Figure 5: Chemical structures of polymers used for PEDOT:PSS preparation. (a) Poly(3,4-ethylenedioxythiophene) (PEDOT). (b) Poly(styrene sulfonate) (PSS). (c) Polytetrafluoroethylen polyethylenglycol block copolymer (Zonyl FS-300).

Poly(3,4-ethylenedioxythiophene) (PEDOT) was first reported as novel electrical conducting polymer by Bayer in 1991 [107]. Poly(styrene sulfonate) (PSS) is an insulating material, which allows the dispersion of PEDOT in aqueous solution. The chemical structures of PEDOT and PSS are shown in Fig. 5 (a) and (b), respectively. The blend component, PEDOT:PSS, is a widely used p-type conductive, flexible polymer and nearly transparent in the visible spectrum of light. This enables its usage as electrode material and as hole transport layer in various electronic components like flexible transistors and thin film solar cells [108]. In this thesis, some MAPI films are processed on PEDOT:PSS. It was reported that perovskite thin film grow denser when applied on the polymer. Improvement of perovskite film growth and enhanced surface coverage can be achieved by using DMSO and Zonyl FS-300 as

additives [109]. The latter is a block copolymer consisting of polytetrafluoroethylen and polyethylenglycol. The chemical structure is shown in Fig. 5 (c). DMSO has the side effect of doping the film and therefore improving the conductivity, which is a desired characteristic for electronic devices [108]. Another advantage of growing MAPI on PEDOT:PSS is the presence of an electrical contact below the perovskite thin film which enables easy implementation into final devices.

2.1.3 Synthesis of methylammonium iodide

An equimolar amount of HI (57 %) is added dropwise to a stirred solution of methylamine in ethanol (33 %) at 0 °C. After complete addition, the solution is stirred at 0 °C for 2 h. The water-ethanol mixture is evaporated under vacuum at 80 °C. The product is filtered and washed with diethylether several times. The precipitate is dried over night at 60 °C in a vacuum oven to achieve a slightly yellowish powder.

2.2 Thin film fabrication

2.2.1 General processing

Glass substrates (1.5 × 1.5 cm, 2.5 × 2.5 cm) or ITO coated glass (2.5 × 2.5 cm), respectively, are cleaned with toluene by using soft wipers. Further cleaning is done with ultra-sonication in ammonia solution (0.2 M) at 80 °C for 15 min. 2 mL hydrogen peroxide solution (30 %) is added to the hot detergent solution and is further sonicated at 80 °C for 15 min. After washing with deionized water three times, the substrates are sonicated in 2-propanol (IPA) for 30 min and blown off with compressed air. The films are processed through spin coating from the respective solution.

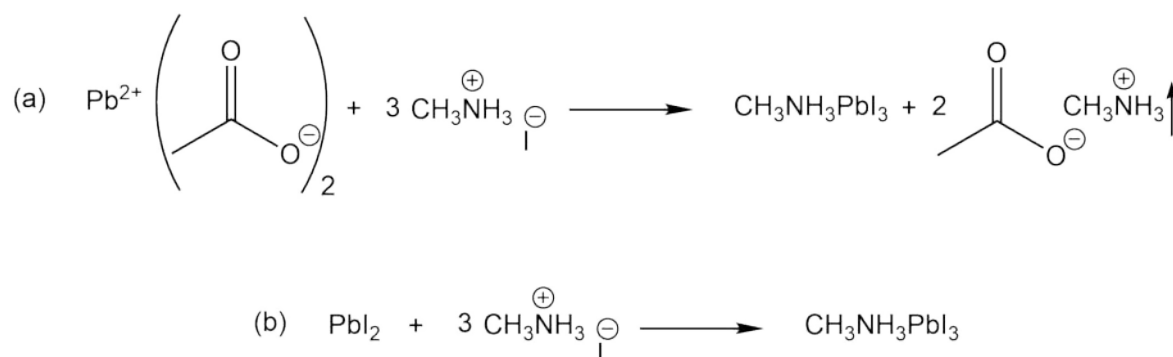
A mixture of 15 mL PH1000, 1 mL DMSO and 2-3 drops Zonyl FS-300 is used for processing the PEDOT:PSS layer. The suspension is spin coated on cleaned substrates (either glass or glass|ITO) in ambient conditions. The spin coating parameters for all applied layers are listed in Table 3. The film is annealed at 120 °C for 15 min. The formed film is washed with IPA to remove excess Zonyl from the PEDOT:PSS surface [109]. The film is then again annealed at 120 °C for 15 min.

For MAPI application, specific optimized recipes and processing conditions are required. An overview of the used recipes from lead iodide precursor solution is listed in Table 5. Also, lead acetate can be used instead of lead iodide for precursor solution (Table 4). All solutions were stirred over night at room temperature. The

Table 3: Spin coating parameters, used for preparation of thin films.

Material	Speed / rpm	Time / s	Ramp / rpm s ⁻¹
PEDOT:PSS	1500	45	750
IPA	2000	2	1000
	4000	15	2000
MAPI	2000	10	1000
	4000	30	2000
TOPO	2000	10	1000
	4000	30	2000
BA	2000	10	1000
	4000	30	2000
PC ₆₀ BM	1320	16	700
	1980	15	900

reaction equations for MAPI formation out of the different precursor mixtures are shown in Fig. 6. The achieved side product from the first preparation route (a), methylammonium acetate, is volatile and evaporates during annealing [17]. The lead acetate recipe can be used only under inert conditions (nitrogen glovebox). The solvent composition and annealing conditions are listed in the same table. Unless otherwise stated, the amount of amine is equivalent to the amount of MAI. For the preparation of heterostructures, the total amine concentration is meant. The ratio x between bulky cation (TPAI, TBAI or THAI) and MAI is then specifically given. All materials including lead acetate trihydrate were used as received.

**Figure 6:** Reaction equation for MAPI formation (a) from lead acetate precursor solution and (b) from lead iodide precursor solution.

2.2 Thin film fabrication

Table 4: Overview of recipes for the preparation of MAPI films from lead acetate precursor solution.

Nr.	Conc.	Precursors	Solvent	Annealing		
		Amine/Pb(OAc) ₂ /PbCl ₂	Name	Ratio	T/ °C	t/ min
R1	1 M	2:0.6:0.067	DMF	1	100	5
R2	1 M	2:0.6:0	DMF/DMSO	4:1	100	5
R3	1 M	2:0.57:0.03	DMF/DMSO	4:1	100	5

Table 5: Overview of recipes for the preparation of MAPI films from lead iodide precursor solution.

Nr.	Conc.	Precursors	Solvent	Annealing		
		Amine/PbI ₂ /PbCl ₂	Name	Ratio	T/ °C	t/ min
R4	0.6 M	1:1:0	DMF/DMSO	4:1	100	5
R5	0.6 M	1.11:1:0.11	DMF/DMSO	4:1	100	5
R6	1 M	2:0.5:0.5	DMF/AA	5.67:1	120	5
R7	1.17 M	2.2:0.5:0.5	DMF/AA	5.67:1	120	5

2.2.2 Anti solvent technique

As already noted, anti solvent treatment is used to improve the crystal quality and surface coverage of the perovskite thin film. Another benefit is the improvement of the film smoothness, which reduces hysteresis and facilitates efficient charge transfer between perovskite and the upper layer in a final device. Residual solvent from the precursor solution is displaced during spin coating by dropwise adding a certain amount of an immiscible liquid on the spinning substrate [18–21].

This technique is applied for all MAPI films prepared during this thesis. Chlorobenzene is used as anti solvent. The dropwise addition of the anti solvent for the MAPI recipe from Table 3 starts at the 20th second (when 20 s are left) and is done within 5 s.

2.2.3 Preparation of methylammonium lead iodide thin films with trioctylphosphine oxide passivation

The MAPI thin film is applied from R1 precursor solution (referring to Table 4) on a pre-scratched glass substrate (2.5 × 2.5 cm). After MAPI application, the substrate is cracked into three parts. For one of the films, no TOPO layer is added on top (bilayer method). The spin coating parameters for TOPO layer application are listed in Table 3.

For the remaining two substrates TOPO is applied once and twice, respectively, as an additional layer from a 0.1 % solution in chlorobenzene. This makes sure that the passivation layer is always applied on the same pristine MAPI film, which facilitates simple comparison. Both layers are processed in inert conditions (nitrogen) at room temperature.

2.2.4 Investigation of methylammonium lead iodide interaction with trioctylphosphine oxide

A pristine MAPI thin film is prepared from R1 precursor solution on glass substrates (Table 4). A chlorobenzene drop is applied on the surface of the film. Another drop from a 0.1 % TOPO solution in chlorobenzene is applied on a different spot. After allowing the drop to dry, the film is investigated under the light microscope (Nikon eclipse LV100ND). The whole experiment is done in nitrogen conditions at room temperature.

2.2.5 Preparation of methylammonium lead iodide thin films with water additive

The MAPI film is processed from R1 precursor solution listed in Table 4 on a 2.5×2.5 cm glass substrate. For this particular precursor solution preparation, lead acetate trihydrate is dried at 50 °C in a vacuum oven to remove the crystal water. 194 μ L precursor solution is mixed with 6 μ L deionized water (Milli-Q 18M Ω) to achieve a 3 % solution. The additive is directly added to the precursor solution and therefore the term monolayer method is used. For the 5 % mixture, 190 μ L precursor solution is mixed with 10 μ L deionized water. The layer is processed in inert conditions (nitrogen glovebox) at room temperature.

2.2.6 Preparation of methylammonium lead iodide thin films with slight excess of a precursor component

For MAPI film application, R4 precursor solution is used. Additionally, solutions with 3 mol% excess of methylammonium iodide (MAI) and 3 mol% excess of lead iodide, respectively, are prepared. The layers are applied on cleaned glass substrates (2.5×2.5 cm) in atmospheric conditions at room temperature.

2.2.7 Preparation of methylammonium lead iodide thin films with lead chloride additive

The influence of lead chloride additive for the lead iodide recipe, as well as for the recipe with lead acetate, is investigated in this experiment. The films are applied on cleaned glass substrates (2.5×2.5 cm).

For MAPI preparation from lead acetate precursor solution, R2 is used for the film without additive. R3 is used for the MAPI layer with lead chloride additive (Table 4). The amine/lead ratio is kept constant. The films are processed in nitrogen atmosphere at room temperature.

R4 and R5 from Table 5 are used for films from lead iodide precursor solution with and without additive, respectively. Also here, the amine/lead ratio is kept constant. The films are fabricated in atmospheric conditions at room temperature.

2.2.8 Preparation of methylammonium lead iodide thin films with benzylamine passivation

The MAPI thin film is applied referred to Table 4 from R1 precursor solution on a pre-scratched glass substrate (2.5×2.5 cm). The substrate is cracked into three parts after MAPI application. One of the parts remains without BA treatment. For the other two substrates BA is applied once and twice, respectively, from a 0.1 % solution in chlorobenzene. The spin coating parameters are listed in Table 3. Both layers are processed in inert conditions (nitrogen) at room temperature.

2.2.9 Preparation of methylammonium lead iodide thin films with tetrabutylammonium iodide additive

A certain amount of the additive TBAI is directly added to R6 precursor solution (monolayer method). The MAI/TBAI ratio x is chosen to be 0, 0.01, 0.02, 0.03, 0.04, 0.05 and 0.1. The amount of TBAI is added from a 2 M solution in DMF/AA (5.67:1). Therefore the lead concentration is slightly reduced. The films are prepared on glass|PEDOT:PSS (1.5×1.5 cm) in inert conditions (nitrogen) at room temperature.

2.2.10 Preparation of methylammonium lead iodide thin films with tetrahexylammonium iodide and tetrabutylammonium iodide additive (combinatory method)

For this experiment, R1 precursor solution is used. The pristine film is processed as usual with chlorobenzene as anti solvent. For two other films, a 0.1 % solution of THAI in chlorobenzene and a 0.01 % solution of TBAI in chlorobenzene, respectively, are used as anti solvent.

Additionally, films with a ratio of THAI/MAI = 0.02 in the precursor solution are prepared. The molar total amine concentration and concentration of the other components are kept constant. For these films, beside simple chlorobenzene treatment, a 0.1 % solution of THAI in chlorobenzene and a 0.01 % solution of TBAI in chlorobenzene, respectively, are used as anti solvent.

The films are processed on 2.5×2.5 cm glass substrates in nitrogen atmosphere at room temperature.

2.2.11 Preparation of methylammonium lead iodide thin films with tetrapropylammonium iodide

R7 precursor solution is used to prepare thin films on glass|PEDOT:PSS (1.5×1.5 cm). For the second solution, which includes the additive TPAI, a amine ratio x of TBAI/MAI = 0.04 is used. The preparation is done in atmospheric conditions at room temperature.

2.3 Solar cell fabrication

ITO glass is pre-patterned by protecting the desired ITO coating with a PVC tape and etching the remnant ITO with HCl (37 %). The substrates are cut (2.5×2.5 cm) and cleaned with the same procedure listed in 2.2.1. PEDOT:PSS, as well as MAPI are deposited with the standard procedure explained in the same section. For the MAPI layer, R7 with an amine ratio x of TPAI/MAI = 0.04 is used. PC₆₀BM is applied from a $20 \frac{\text{mg}}{\text{mL}}$ solution in chlorobenzene. The procedure was done in ambient conditions at room temperature. Al (100 nm) is deposited by vacuum evaporation (Edwards Auto 500).

2.4 Photoluminescence

Photoluminescence (PL) is measured by exciting MAPI thin films on either glass or glass/PEDOT:PSS with a laser (Coherent Obis, excitation wavelength = 488 nm, power = 5 mW). Two long-pass filters are used for shielding the excitation light (515 nm, 550 nm). A CCD sensor attached to a Shamrock 303i monochromator equipped with 150 lines/mm, blaze 800 nm grating is used to acquire the emitted photoluminescence (Andor DV420A-OE).

2.5 IV-characterization

The solar cells are measured under AM1.5G spectrum (LOT-Quantum Design: Xenon arc lamp with filter) by changing the voltage from -1 to 1.5 V and detecting the current using a source measure unit (Keithley 2401 Source Meter). The intensity of the simulated sun is determined with a calibrated silicon solar cell (Mencke&Tegtmeyer).

2.6 UV-VIS spectroscopy

Transmittance T of MAPI thin films on glass/PEDOT:PSS is measured with Perkin Elmer Lambda 1050 UV/Vis/NIR spectrometer (double beam) between 490 - 840 nm. The machine is equipped with three detectors: Photomultiplier tube, InGaAs detector and PbS detector. The absorbance is calculated according IUPAC by using the negative decadic logarithm of the transmittance.

2.7 Scanning electron microscopy

For Scanning Electron Microscopy (SEM), JEOL JSM-6360 LV microscope with Bruker Nano X-Flash detector was used. MAPI thin films on glass|PEDOT:PSS, are measured with an acceleration voltage of 7 keV.

3 Results and discussion

The goal of this thesis is to enhance the photoluminescence of methylammoniumlead iodide thin films which is achieved by using specialized fabrication techniques and the introduction of additives into the recipe. The added substances can improve the perovskite layer formation and seal recombination centers in the bulk and at the surface. Each additive can influence the MAPI layer in a specific way, therefore the classification into three passivation mechanisms (coordinate bonding, ionic bonding and conversion to layered structures) is chosen. For all processed layers, anti solvent technique is applied, since a visual improvement of the layers could be achieved. This simplifies the comparison and assessment of the films investigated with *PL* measurements.

3.1 Coordinate bonding

The passivation through coordinate bonding is investigated by using TOPO and water. TOPO behaves as Lewis base and can therefore coordinate to electron poor lattice defects. Water has ambivalent characteristics, depending on the surrounding conditions. It can coordinate to electron poor, as well as to electron rich parts of the crystal.

3.1.1 Influence of trioctylphosphine oxide

The results for TOPO utilization clearly reveal a passivation effect on the perovskite thin film. A remarkable increase of the signal shown in Fig. 7 (a) is achieved by applying TOPO layers on the perovskite thin film. The electronegative oxygen act as electron donor and can give its lone pair to the undercoordinated Pb^{2+} to form a coordinative bond [27, 39]. As a consequence, the surface recombination states are reduced due to the passivation of defects. A schematic illustration of TOPO occupying a defect is shown in Fig. 7 (b). However, the number of TOPO applications is limited, since the additive does not only passivate, but also degrade the material. This phenomenon is shown on the microscope pictures in the same figure. Fig. (c) corresponds to the picture of the pristine film with the dried chlorobenzene drop on it. (d) shows the dried TOPO drop from a chlorobenzene solution. The TOPO solution destroyed the MAPI film immediately after application, suggesting that the molecule cannot only passivate surface recombination states, but can also migrate into the perovskite bulk. By controlling the amount of TOPO applied on top, an ideal concentration for passivation can be achieved. This makes TOPO a promising

3.1 Coordinate bonding

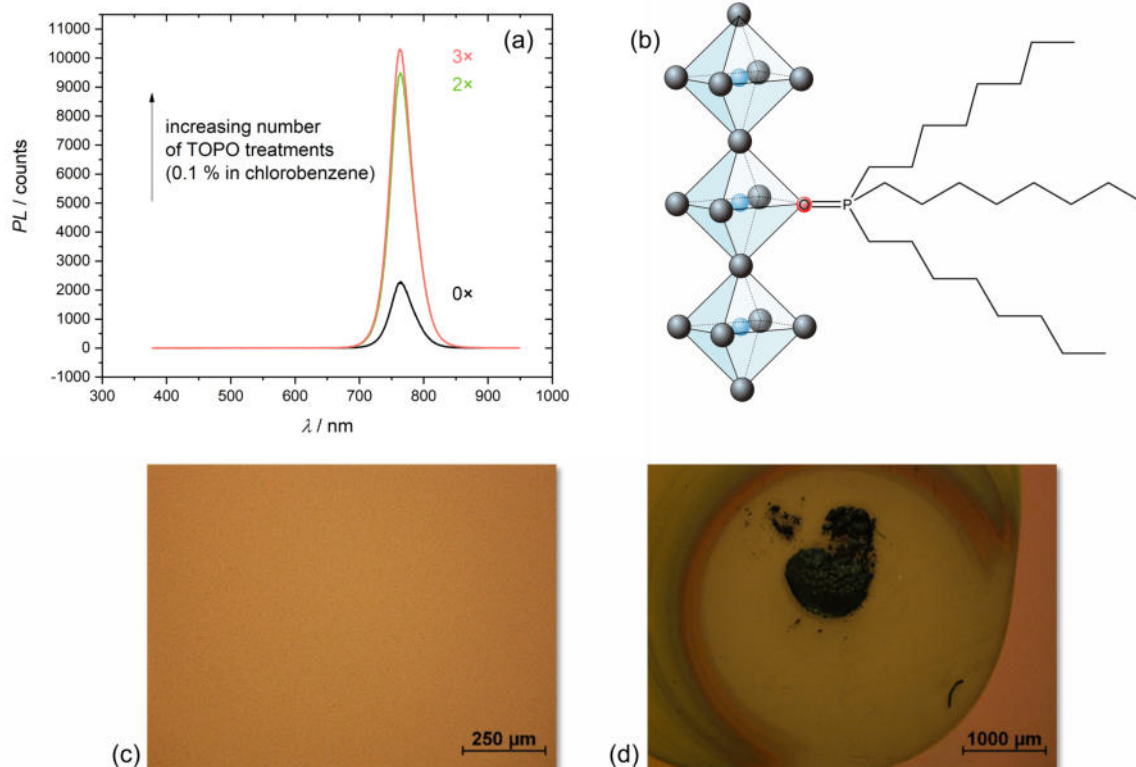


Figure 7: Passivation of a MAPI thin film on glass from lead acetate precursor solution with TOPO treatment. The signals are measured with a slit width of 100 μm and with an exposure time of 1E-5 s (a) Photoluminescence of a pristine MAPI thin film and MAPI films with TOPO passivation. (b) Schematic illustration of TOPO occupying an empty space at the surface of the MAPI crystal. (c) Microscope picture of a pristine MAPI film, treated with chlorobenzene. (d) Microscope picture of a pristine MAPI film after intense TOPO treatment.

candidate for sealing imperfections at the perovskite surface. Still, the implementation of TOPO in an electronic device could be quite challenging. The long alkyl chains have insulating properties and can hinder the charge transport to the electrodes [39]. Therefore, to use this material for certain applications like solar cells, more investigations are necessary.

3.1.2 Influence of water

The controlled addition of water into the precursor solution shows a distinct impact on the formed MAPI film. The coordinate bonding between the perovskite lattice and water might either be formed by water acting as a Lewis base (H_2O , HO^-), or by a proton obtained from dissociation and acting as Lewis acid. The *PL* changes

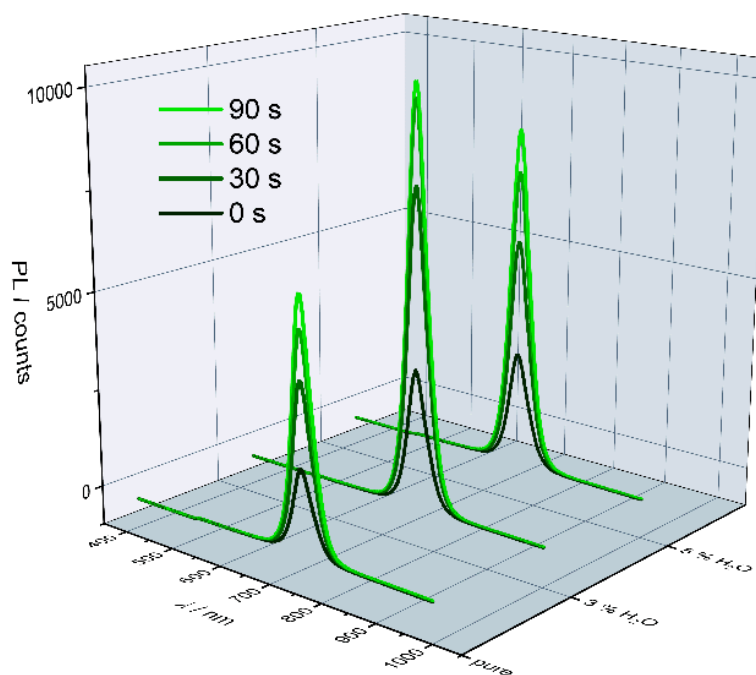


Figure 8: Photoluminescence of MAPI thin films on glass from lead acetate precursor solutions with 0 %, 3 % and 5 % water, respectively, measured after 0 s, 30 s, 60 s and 90 s of illumination with a slit width of 100 μm and an integration time of 1 s.

drastically during recording. The first signal is taken right after switching on the laser. Further signals are taken after 30 s, 60 s and 90 s of illumination. The *PL* measurements are shown in Fig. 8. After switching off the laser, the measurement is repeated again. The *PL* signals again showed the same behaviour upon illumination, starting from the same intensity as detected before. This indicates a reversible change of the signal over time triggered by illumination, which would lead to a so-called light soaking effect in the final device. The effect describes the change of the measured power conversion efficiency in solar cells over time of light exposure [110]. This phenomenon not only occurs for the MAPI layers with water additive, but also for the pristine film. It is regularly observed when using the recipes with lead acetate as primary material. However, the change of the *PL* signal is stronger for the films with water, suggesting that the light soaking effect might correlate to the presence of water in the MAPI film. The samples are not stored at inert conditions, therefore absorption of water (and oxygen) by the pristine film is highly probable. Even for an encapsulated p-i-n perovskite solar cell, one cannot fully exclude the presence of water. For example, PEDOT:PSS can easily absorb moisture, which can migrate to the perovskite bulk [111]. Water might also play an important role for the overall stability of the device, due to its participation in the MAPI decomposition

pathway [26].

3.2 Ionic bonding

The role of Pb^{2+} and Methylammonium⁺ in MAPI thin films is examined by adding a slight excess of the components, used for the precursor solution. To keep the total amount of iodide constant, the recipe with lead iodide as lead source is used. For investigating the influence of chloride, lead chloride is introduced into both recipe types (with lead iodide and lead acetate as precursor components). An illustration of anion incorporation into halide vacancies is shown in Fig. 9 (a). A cation can either occupy lead vacancies or intercalate between the octahedrons and compensate MA^+ vacancies as shown in (b).

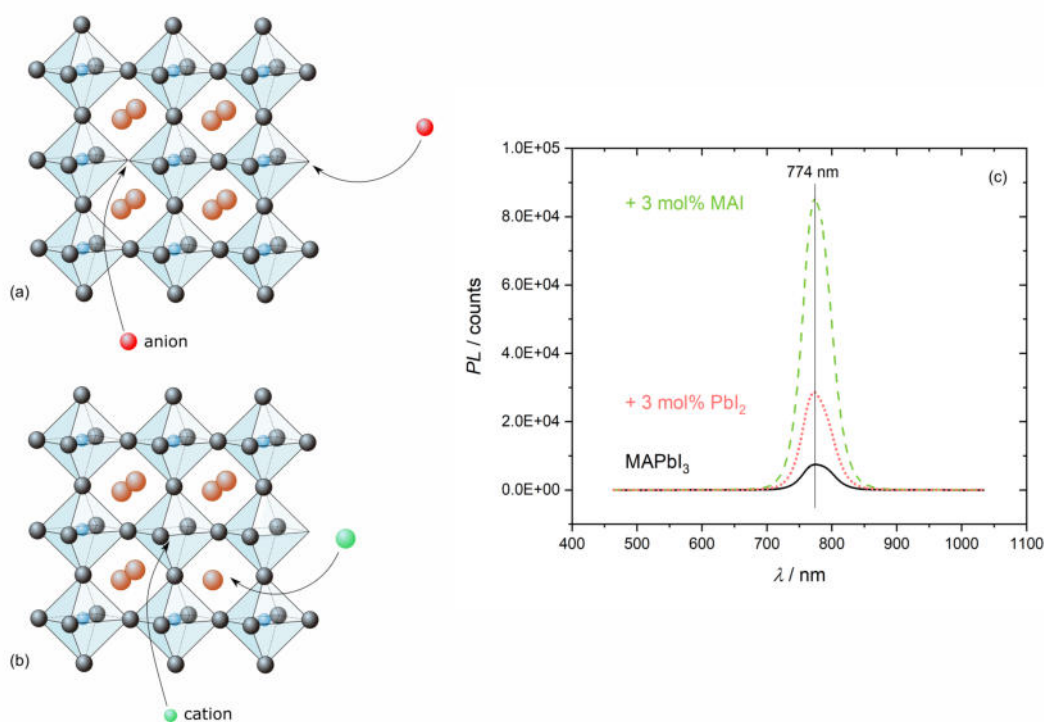


Figure 9: Possible mechanism of anion (a) and cation (b) implementation into the perovskite lattice. (c) Photoluminescence of MAPI thin films on glass from a $\text{MAI}/\text{PbI}_2 = 1:1$ precursor solution and from solutions with slight excess of one of the precursor components. The signals are normalized to an input slit width of $100 \mu\text{m}$ and measured with an integration time of 1 s.

3.2.1 Influence of lead iodide and methylammonium iodide in slight excess

A slight excess of 3 mol% PbI_2 and 3 mol% MAI, respectively, leads both to an enhancement of the *PL*. The resulting curves are shown in Fig. 9. An excess of MAI seems to have a stronger positive impact on the perovskite film formation. Lead ions and Methylammonium can passivate electron rich defects like undercoordinated I^- , antisite PbI_3^- and methylammonium vacancies by electrostatic interaction. Iodide can interact with undercoordinated lead ions or incorporate into iodide vacancies [46]. Therefore the trap concentration in the MAPI thin film is lowered, which consequently increases the probability of radiative recombination. A decrease of the defect concentration by using excess of lead iodide in the OIHP precursor solution is also reported in literature [8], which accentuates the suggestion. Excess MAI might be deposited on the grain boundaries and form a passivating layer [80].

3.2.2 Influence of lead chloride and comparison of recipes

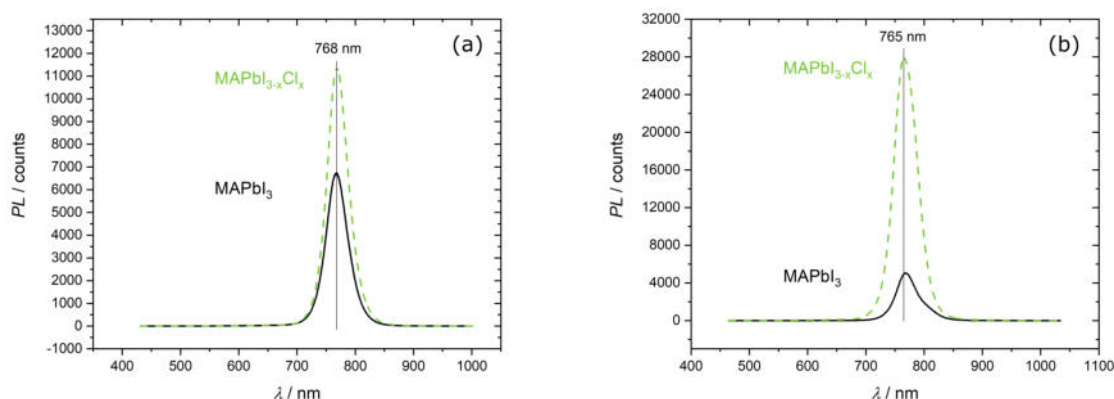


Figure 10: Photoluminescence of MAPI thin films on glass prepared (a) from a recipe with lead acetate as lead source, measured with an input slit width of 10 μm and at an exposure time of 1 s and (b) from a recipe with lead iodide as lead source, measured with a slit width of 100 μm at 1 s exposure time.

The results for the introduction of lead chloride to the precursor solution are shown in Fig. 10. For both recipes, an increase of the *PL* signal is achieved, which means that chlorine shows a positive effect on the MAPI film formation. The interaction between chloride and the perovskite lattice may take place through undercoordinated lead ions or iodide vacancies [46]. This is the first recipe where a solvent mixture (DMF/DMSO = 4:1) is used for the solution. For all films prepared with DMSO (as well as with AA) a more homogeneous, denser film and higher *PL* is noticed.

3.2 Ionic bonding

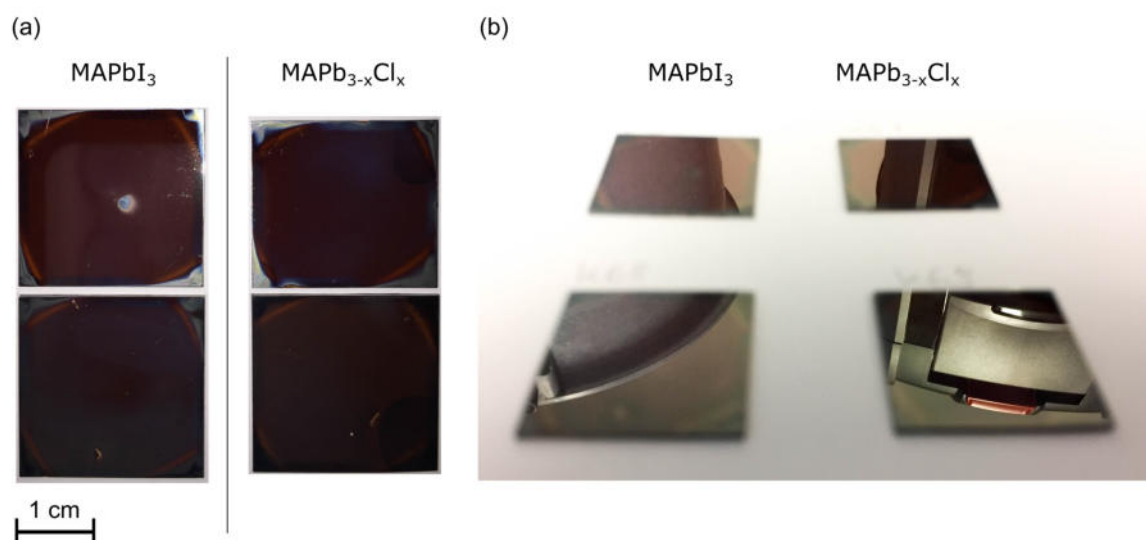


Figure 11: (a) Top view of two MAPI layers on glass prepared by using lead acetate recipe without chloride additive (left) and two films with lead chloride (right). (b) Side view of the films in the same order.

Within this chapter, also the differences between the two recipes used for MAPI preparation are discussed. In general, films from the lead iodide precursor solution are found to give a particularly higher *PL* signal when processed on PEDOT:PSS. For films applied on glass substrates, the signal of the MAPI film from lead acetate precursor solution is found to be slightly higher. The films from lead acetate precursors appear optically shiny with a very small number of pin holes, which has already been described in the literature [17]. This might correlate to the delayed crystal formation,

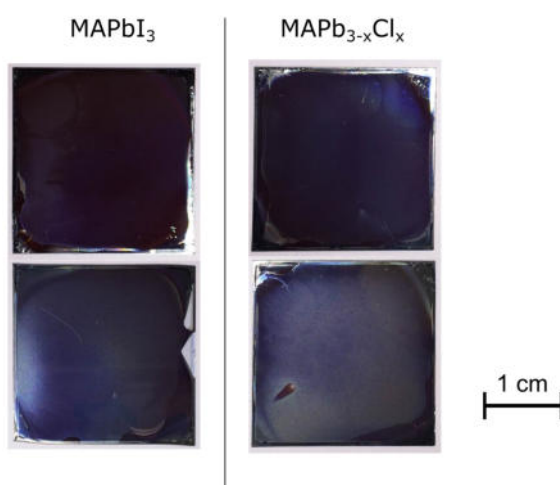


Figure 12: Top view of two MAPI thin films on glass prepared by using lead iodide recipe without chloride additive (left) and two films with lead chloride (right).

3.3 Conversion to layered structures

since methylammonium acetate needs to leave the film during annealing. Photos of these layers, with and without lead chloride additive, are shown in Fig. 11. There is no optical difference between the layers with and without additive, which accentuates the suggestion, that the chlorine contributes to the enhanced *PL*.

The films prepared from lead iodide precursor solution are shown in Fig. 12. The films are much rougher compared to the films from lead acetate precursor solution. This makes them more difficult to characterize and also for solar cell applications, the roughness of the film might have a negative impact for charge carrier extraction.

3.3 Conversion to layered structures

In this chapter, the conversion of surface trap states to energy states, that are located outside of the band gap, is discussed. For the investigation, bulky cations, that can exchange with the A cation from perovskite lattice (MA^+), are introduced in the fabrication process. The octahedron layers are therefore hindered to stuck on each other and layered structures are formed. These layered structures show a larger band gap compared to pristine MAPI. As additional layer, BA is applied on top of a pristine perovskite layer. Three tetraalkylammonium salts are introduced to the preparation procedure with different techniques.

3.3.1 Influence of benzylamine

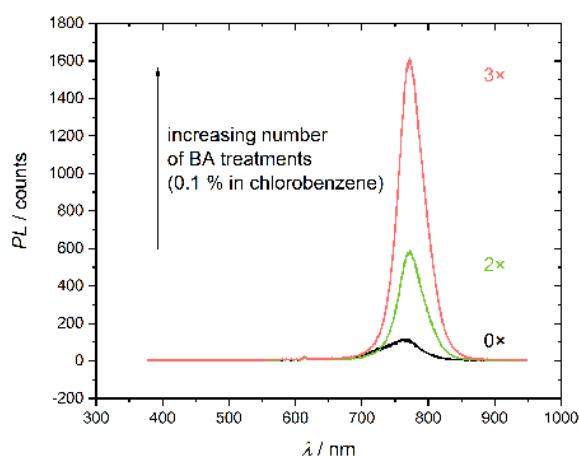


Figure 13: Photoluminescence signal of a pristine MAPI thin film and MAPI films with BA passivation, prepared from lead acetate precursor solution on glass. The signals are measured with an input slit width of 100 μm and an integration time of 0.5 s.

3.3 Conversion to layered structures

The results shown in Fig. 13 clearly reveal an increase of the *PL* signal upon BA application on top of a pristine MAPI film. On the one hand, BA interacts with the perovskite crystal due to the Lewis base characteristics of the nitrogen atom. On the other hand, at higher concentrations, the molecule can intercalate into the lattice to form heterostructures. Similar to TOPO, here the number of possible treatments is also limited, since the amount of absorber material is reduced during conversion.

3.3.2 Influence of tetrabutylammonium iodide

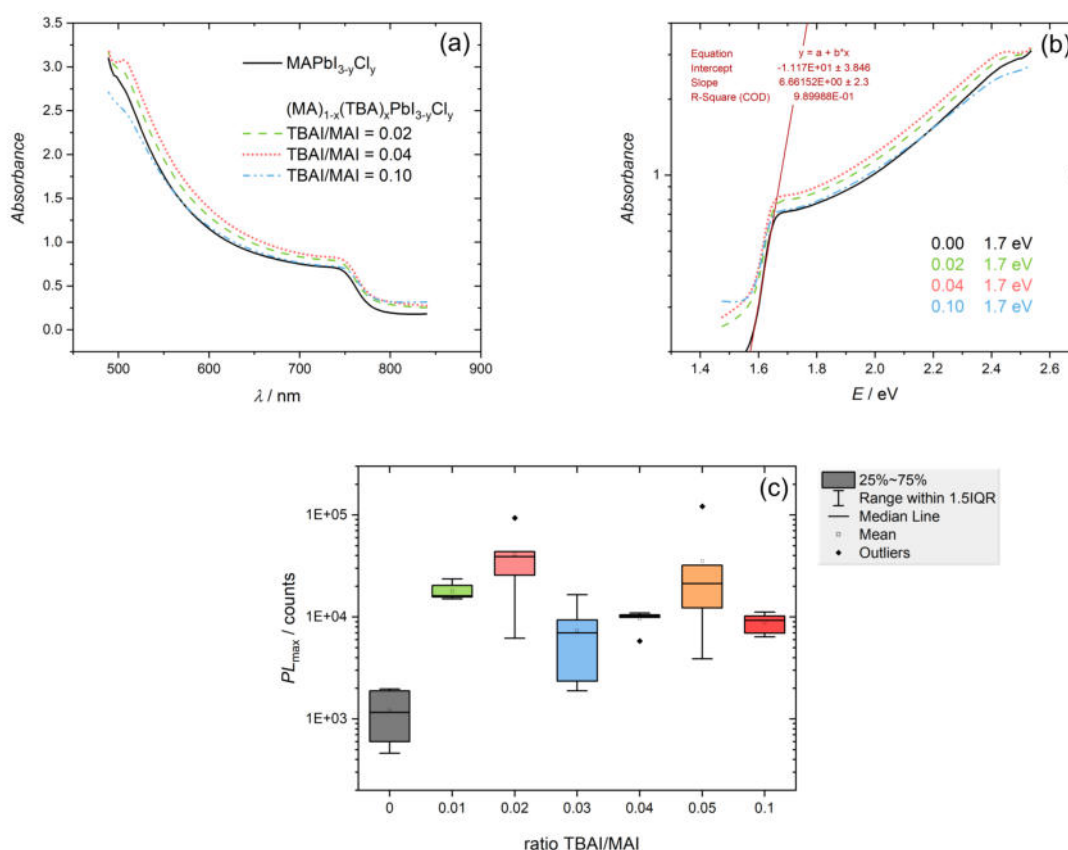


Figure 14: MAPI thin films on PEDOT:PSS, prepared from lead iodide precursor solutions with different TBAI/MAI ratio. (a) Absorbance as a function of wavelength. (b) Absorbance as a function of photon energy on a logarithmic scale. (c) Error Bar diagram of peak intensity PL_{max} as a function of TBAI/MAI ratio in the precursor solution. The *PL* signals are measured with an input slit width of 100 μ m and an integration time of 0.1 s.

Different amounts of TBAI are added to a MAPI precursor solution for investigation. The lead concentration of the modified solutions is slightly reduced, due to addition of the additive. This should not have a huge influence, because of the already

3.3 Conversion to layered structures

large amine excess used in this recipe. To take a closer look at the reproducibility, $n = 6$ films are prepared for each concentration. As already mentioned, MAPI from lead iodide solution shows a higher PL when applied on PEDOT:PSS films. This leads to the suggestion that MAPI, fabricated from lead iodide precursors, in general grows better on PEDOT:PSS compared to glass. This phenomenon is also stated in literature [109]. Fig. ?? (a) and (b) show the quite similar absorbance of certain concentrations of the MAPI thin films in nm and eV, respectively. The optical band gap is determined by generating a linear fit at the beginning of the absorption spectra, as shown for the black curve in (b). The calculated values are relatively similar to each other, which indicates that the bulky cation is not dispersed in the semiconductor bulk, but pushed to the surface. This is also suggested in literature [7, 68, 92]. For a better overview, the peak intensity PL_{\max} of the prepared thin films is plotted as a function of TBAI/MAI ratio in the precursor solution (Fig. ?? (c)). It is assumed that the absorption coefficient and reflectance of all films are nearly the same, due to the identical fabrication procedure. A remarkable increase of the PL signal is achieved by adding any amount of TBAI. The highest values are measured for films with a TBAI/MAI ratio of 0.02. In some rare cases, outliers are observed, which show a much higher PL signal compared to the identical other films prepared from the same solution and with the same procedure. Further investigations are required to achieve a stable recipe from which films with much higher PL quantum efficiency can be prepared.

The data from PL_{\max} is plotted as a function of TBAI/MAI concentration in a 2D multivariate Kernel density estimation (KDE) graph (Fig. 15). The density in this graph corresponds to the estimated probability of a certain value. KDE is used as a non-parametric statistical tool to smooth data and interpret the shape of random data sets. KDE is calculated by weighting the distance of all data points. The darker the area, the higher the probability of finding a data point there. From this graph one can draw conclusion, that high PL values can be achieved by adding an additive concentration below 0.10, or more accurate, in the range between 0.01 and 0.05.

3.3 Conversion to layered structures

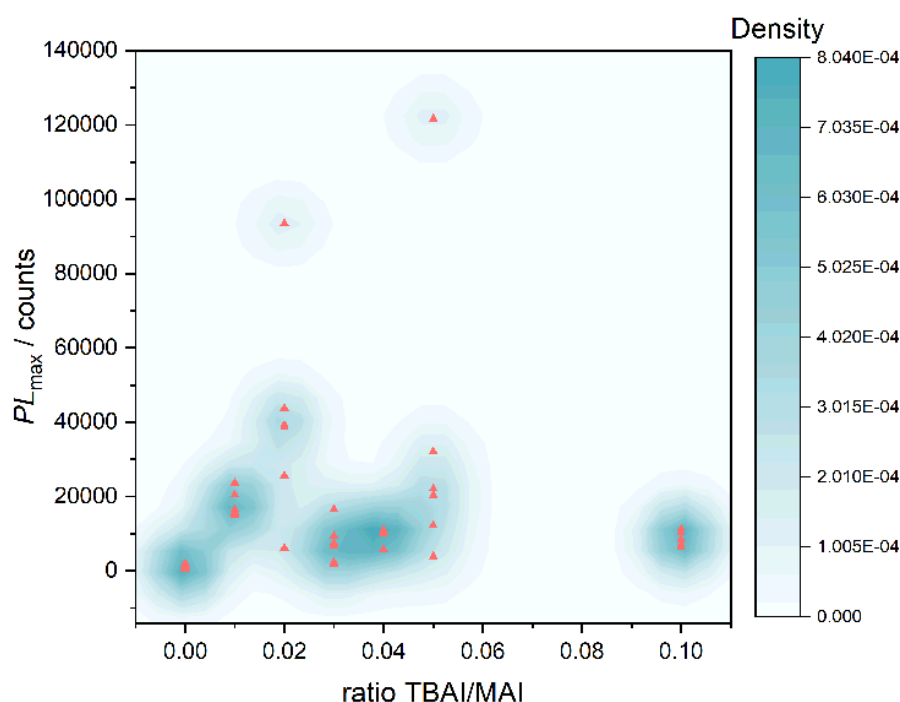


Figure 15: Multivariate Kernel density estimation of peak intensity PL_{\max} of MAPI thin films as a function of TBAI/MAI ratio in the precursor solution. The PL signals are measured with an input slit width of 100 μm and an integration time of 0.1 s.

3.3.3 Influence of tetrabutylammonium iodide and tetrahexylammonium iodide combinations

In this experiment, the additive is dissolved in chlorobenzene and applied during spin coating as anti solvent. Already for the pristine precursor solution, an enhancement of the PL signal is achieved upon applying the additive solution (Fig. 16). The intensity is comparable with the intensity of the signal for the $(\text{MA})_{1-x}(\text{THA})_x\text{PbI}_{3-y}\text{Cl}_y$ film with simple chlorobenzene anti solvent treatment. The signal gets even higher when combining the usage of the additive in the precursor solution and as anti solvent. This clearly reveals, that the usage of TBAI and THAI can positively influence the perovskite layer in several possible combinations. However, in a final device the use of additives with short alkyl chain length might be preferable. The longer the alkyl chain, the stronger the insulating character of the molecule. Therefore the charge transport is hindered when implementing long alkyl chains into the device. As both, TBAI and THAI, affect the perovskite film to a comparable extent, the use of TBAI is preferred because of the shorter alkyl chains.

3.4 Implementation of an additive into a solar cell

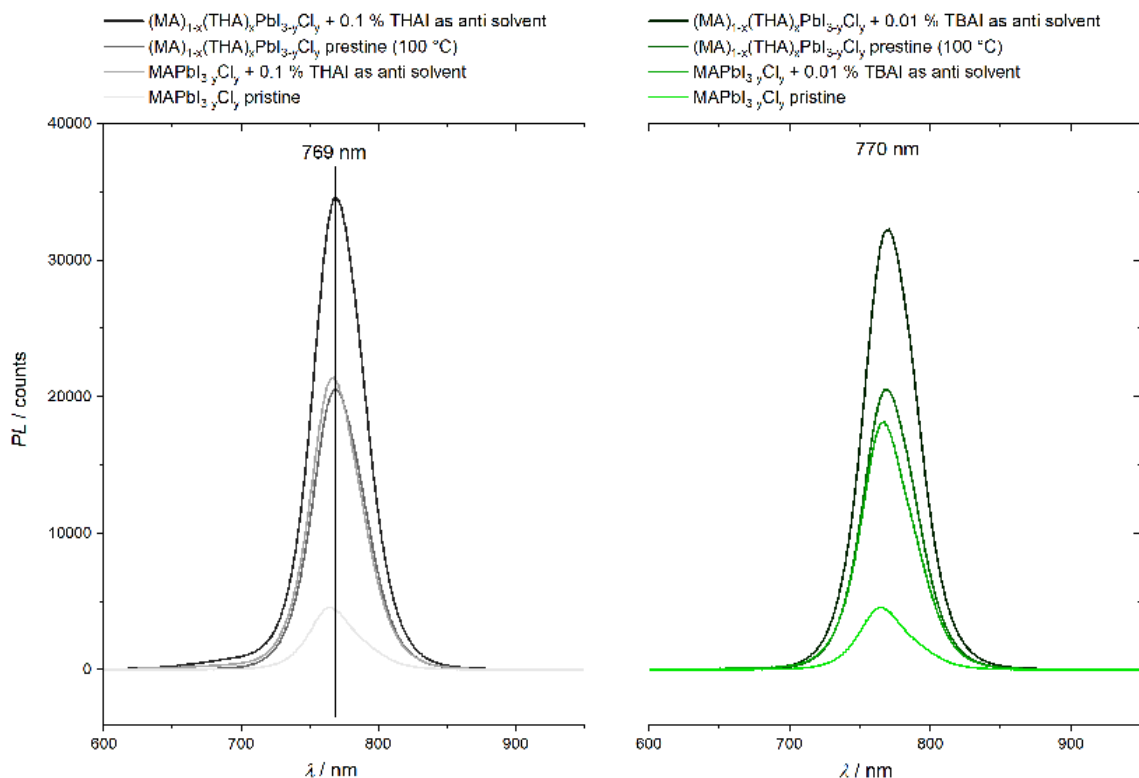


Figure 16: Photoluminescence of MAPI thin films applied from lead acetate precursor solution on glass substrates. The films are prepared by using different application techniques for the passivating agents, TBAI and THAI. The signals are measured with a slit width of 100 μm and an exposure time of 0.2 s.

3.4 Implementation of an additive into a solar cell

TPAI is investigated by incorporation into a photovoltaic device. This additive is chosen because the usage of alkylammonium salts led to strong *PL* enhancement. The bulky cations might be located at the surface and can passivate each individual grain [7, 68, 92]. This makes heterostructure formation a promising technique for sealing non-radiative surface states. Another aspect is that the shorter alkyl chains of TPAI might facilitate more efficient charge transport, compared to long-chained TBAI and THAI [92]. Also, the large excess of MAI used in this recipe contributes to passivation of surface states [80].

Different amounts of TPAI are added to a lead iodide precursor solution for the investigation of a thin MAPI film. Here again, the usage of a bulky A cation leads to an enhanced *PL* signal as shown in Fig. 17 (a). The SEM pictures in Fig. 17 (b) show better surface coverage of films from the solution without additive. A solar cell in the configuration glass|ITO|PEDOT:PSS|(MA)_{1-x}(TPA)_xPb_{1-3-y}Cl_{3-y}|PC₆₀BM|Al (illustrated in

3.4 Implementation of an additive into a solar cell

Fig. 17 (c) reached an open circuit voltage of 940 mV, which is about 100 mV lower compared to values from literature [8, 24, 25, 30, 47, 80]. Further optimization of the device is still necessary to achieve an improvement of the open circuit potential V_{OC} . Also, an optimization of the surface coverage is important, since it is an important to achieve high short circuit current I_{SC} , fill factor FF and consequently a higher power conversion efficiency PCE .

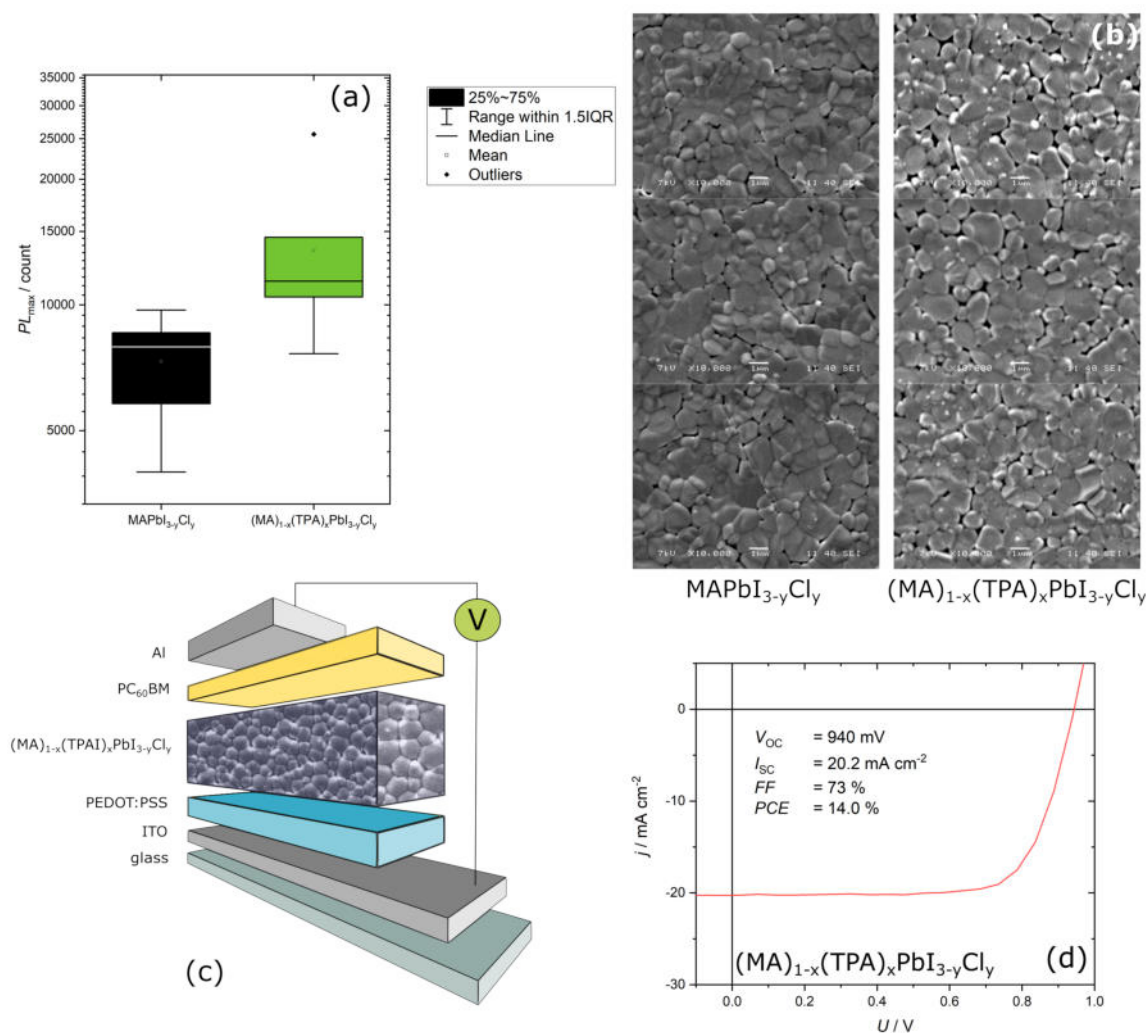


Figure 17: MAPI thin films prepared out of lead iodide precursor solutions with and without TPAI additive. The films are applied on PEDOT:PSS and measured with a slit width of 100 μm and an integration time of 1 s. (a) Error Bar diagram of peak intensity PL_{max} of a pristine film and a film with additive TPAI. (b) SEM pictures of pristine films and films with TPAI additive. (c) Schematic illustration of a p-i-n perovskite solar cell in the configuration glass|ITO|PEDOT:PSS| $(MA)_{1-x}(TPA)_xPbI_{3-y}Cl_y$ | $PC_{60}BM$ |Al. (d) I-V-characteristics of a solar cell in the same configuration.

4 Conclusion and outlook

Among other characteristics, a high open circuit voltage is a prerequisite for highly efficient solar cells. A material giving a high photoluminescence indicates a good absorber and consequently contributes to an improved value for the open circuit voltage and high overall efficiency of the final device. The challenge of enhancing the photoluminescence and therefore generating an optimal absorber layer includes elimination of possible recombination centers. Therefore, optimized fabrication techniques and the usage of additives are necessary to get the best out of OIHP devices. Beside that several other advantages are associated with passivation, like improved device stability and suppression of impurity migration. In this thesis, additives like DMSO and AA were implemented to the perovskite precursor recipe to alter the film forming kinetics and ensure the growth of a dense and uniform film. The anti solvent technique has a similar effect on the film formation and was therefore also used in this thesis. Two different precursor recipes were investigated, one based on lead iodide, the other on lead acetate. The highest *PL* signals were achieved for films prepared from lead iodide precursor solution on glass|PEDOT:PSS.

Several additives that remain in the perovskite after processing, were tested. They are classified into three groups, due to their different impact on the perovskite structure. The passivation via coordinate bonding was investigated by the application of trioctylphosphine oxide on top of a MAPI thin film. It showed a remarkable enhancement of the *PL* signal. Further investigations are necessary for the implementation of this material for solar cell applications. Water also showed to give a higher *PL*, but it is under strong suspicion of causing light soaking effect. It is suspected, that the presence of water contributes to light soaking, which is often obtained for perovskite devices.

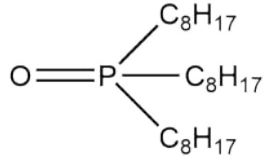
The importance of additional small inorganic ions in the perovskite lattice was investigated by adding an excess of lead iodide, methylammonium iodide and by the addition of lead chloride to the precursor solution. Thereby, lead chloride was implemented to both recipes. All additives seem to passivate the MAPI layer, which is reflected in the increased *PL* signals. Here, the interaction between the additive and the perovskite is suggested to take place by forming an ionic bond.

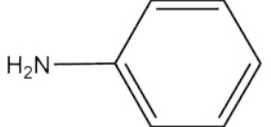
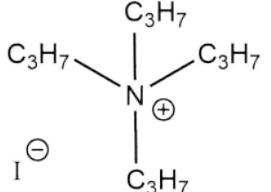
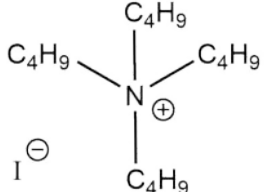
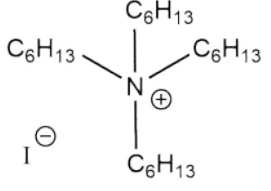
The formation of heterostructures showed to be a highly promising passivation method. As additive, bulky cations are used which can occupy the place of the A cation in the perovskite lattice. As a consequence, the octahedra are getting

segregated and a layered structure is formed that might seal the surface of the perovskite. The tested materials include benzylamine, tetrapropylammonium iodide, tetrabutylammonium iodide and tetrahexylammonium iodide. The additives can be used in various combinations and all seem to have a positive impact on the photoluminescence.

The measurement of photoluminescence is a quick and informative method and requires a relatively simple experimental setup. To draw on the insights achieved within this thesis, the absorber materials should be implemented into completed devices. The evaluation of the open circuit voltage and the electroluminescence *EL* could contribute to a better understanding of the investigated substances. Beside that, many other promising passivation materials exist, which are worthy exploring.

Table 6: Overview of investigated passivation agents for MAPI thin films, including their abbreviation, chemical structure, active functional group, passivation target and reference from literature.

Passivation Agent	Abbr.	Structure	Active Functional Group	Passivation Target	Ref.
Trioctylphosphine oxide	TOPO		Phosphine oxide	Undercoordinated Pb ²⁺	[1, 112]
Water	-	H ₂ O	Water	Undercoordinated Pb ²⁺	[59, 60]
Methylammonium iodide	MAI		Ammonium	Undercoordinated I ⁻ , antisite Pbl ₃ ⁻ , MA ⁺ vacancies	[80]
			Iodide	Undercoordinated Pb ²⁺ , halide vacancies	
Lead iodide	-	Pbl ₂	Lead ion	Undercoordinated I ⁻ , antisite Pbl ₃ ⁻ , MA ⁺ vacancies	[8]
			Iodide	Undercoordinated Pb ²⁺ , halide vacancies	
Lead chloride	-	PbCl ₂	Lead ion	Undercoordinated I ⁻ , antisite Pbl ₃ ⁻ , MA ⁺ vacancies	[73]
			Chloride	Undercoordinated Pb ²⁺ , halide vacancies	

Passivation Agent	Abbr.	Structure	Active Functional Group	Passivation Target	Ref.
Benzylamine	BA		Amine	Undercoordinated Pb ²⁺ , Pb cluster	[69]
Tetrapropylammonium iodide	TPAI		Ammonium	Undercoordinated I ⁻ , antisite Pbl ₃ ⁻ , MA ⁺ vacancies	[113]
Tetrabutylammonium iodide	TBAI		Ammonium	Undercoordinated I ⁻ , antisite Pbl ₃ ⁻ , MA ⁺ vacancies	[7]
Tetrahexylammonium iodide	THAI		Ammonium	Undercoordinated I ⁻ , antisite Pbl ₃ ⁻ , MA ⁺ vacancies	-

List of Abbreviations

AA	Acetylacetone
BA	Benzylamine
BA	Benzylamine
CB	Chlorobenzene
DMF	Dimethylformamide
DMSO	Dimethylsulfoxide
<i>EL</i>	Electroluminescence
IPA	2-Propanol
ITO	Indium tin oxide
KDE	Kernel Density Estimation
MA	Methylamine
MAI	Methylammonium iodide
MAPI	Methylammoniumlead iodide
OIHP	Organic-inorganic halide perovskite
<i>PCE</i>	Power conversion efficiency
PEDOT:PSS	poly(3,4-ethylenedioxythiophene):poly(styrenesulfonate)
<i>PL</i>	Photoluminescence
SEM	Scanning Electron Microscopy
TBAI	Tetra-n-butylammonium iodide
THAI	Tetra-n-hexylammonium iodide
TPAI	Tetra-n-propylammonium iodide
TOPO	Trioctylphosphine oxide

List of Figures

1	(a) Schematic illustration of electron-hole-pair generation via light absorption and reversible reaction for photon generation. (b) Energy diagram for the involved energy states in the absorption process of a photon. η_e ... electrochemical potential of electrons, $\mu_{e,0}$... chemical potential of electrons, $\frac{n_e}{N_C}$... n-doping concentration, η_h ... electrochemical potential of holes, $\mu_{h,0}$... chemical potential of holes, $\frac{n_h}{N_V}$... p-doping concentration	9
2	Schematic illustration of recombination mechanism in a p-i-n perovskite solar cell. (a) Recombination via shallow level traps. (b) Recombination via deep level traps. (c) Recombination via surface states continuously distributed over the energy gap.	11
3	(a) Simple methylammonium lead iodide structure and energy diagram with illustrative dangling bonds between the perovskite-PEDOT:PSS-interface. (b) Two-dimensional perovskite with intercalated tetrabutylammonium molecules between the octahedra and energy diagram with type-I alignment via conversion of pristine perovskite structure to wide band gap semiconductors.	16
4	Perovskite structure in ABX_3 configuration.	19
5	Chemical structures of polymers used for PEDOT:PSS preparation. (a) Poly(3,4-ethylenedioxythiophene) (PEDOT). (b) Poly(styrene sulfonate) (PSS). (c) Polytetrafluoroethylen polyethylenglycol block copolymer (Zonyl FS-300).	20
6	Reaction equation for MAPI formation (a) from lead acetate precursor solution and (b) from lead iodide precursor solution.	22
7	Passivation of a MAPI thin film on glass from lead acetate precursor solution with TOPO treatment. The signals are measured with a slit width of 100 μm and with an exposure time of 1E-5 s (a) Photoluminescence of a pristine MAPI thin film and MAPI films with TOPO passivation. (b) Schematic illustration of TOPO occupying an empty space at the surface of the MAPI crystal. (c) Microscope picture of a pristine MAPI film, treated with chlorobenzene. (d) Microscope picture of a pristine MAPI film after intense TOPO treatment.	29
8	Photoluminescence of MAPI thin films on glass from lead acetate precursor solutions with 0 %, 3 % and 5 % water, respectively, measured after 0 s, 30 s, 60 s and 90 s of illumination with a slit width of 100 μm and an integration time of 1 s.	30

9	Possible mechanism of anion (a) and cation (b) implementation into the perovskite lattice. (c) Photoluminescence of MAPI thin films on glass from a MAI/PbI ₂ = 1:1 precursor solution and from solutions with slight excess of one of the precursor components. The signals are normalized to an input slit width of 100 μm and measured with an integration time of 1 s.	31
10	Photoluminescence of MAPI thin films on glass prepared (a) from a recipe with lead acetate as lead source, measured with an input slit width of 10 μm and at an exposure time of 1 s and (b) from a recipe with lead iodide as lead source, measured with a slit width of 100 μm at 1 s exposure time.	32
11	(a) Top view of two MAPI layers on glass prepared by using lead acetate recipe without chloride additive (left) and two films with lead chloride (right). (b) Side view of the films in the same order.	33
12	Top view of two MAPI thin films on glass prepared by using lead iodide recipe without chloride additive (left) and two films with lead chloride (right).	33
13	Photoluminescence signal of a pristine MAPI thin film and MAPI films with BA passivation, prepared from lead acetate precursor solution on glass. The signals are measured with an input slit width of 100 μm and an integration time of 0.5 s.	34
14	MAPI thin films on PEDOT:PSS, prepared from lead iodide precursor solutions with different TBAI/MAI ratio. (a) Absorbance as a function of wavelength. (b) Absorbance as a function of photon energy on a logarithmic scale. (c) Error Bar diagram of peak intensity PL_{max} as a function of TBAI/MAI ratio in the precursor solution. The PL signals are measured with an input slit width of 100 μm and an integration time of 0.1 s.	35
15	Multivariate Kernel density estimation of peak intensity PL_{max} of MAPI thin films as a function of TBAI/MAI ratio in the precursor solution. The PL signals are measured with an input slit width of 100 μm and an integration time of 0.1 s.	37
16	Photoluminescence of MAPI thin films applied from lead acetate precursor solution on glass substrates. The films are prepared by using different application techniques for the passivating agents, TBAI and THAI. The signals are measured with a slit width of 100 μm and an exposure time of 0.2 s.	38

- 17 MAPI thin films prepared out of lead iodide precursor solutions with and without TPAI additive. The films are applied on PEDOT:PSS and measured with a slit width of 100 μm and an integration time of 1 s. (a) Error Bar diagram of peak intensity PL_{max} of a pristine film and a film with additive TPAI. (b) SEM pictures of pristine films and films with TPAI additive. (c) Schematic illustration of a p-i-n perovskite solar cell in the configuration glass|ITO|PEDOT:PSS|(MA)_{1-x}(TPA)_xPbI_{3-y}Cl_y|PC₆₀BM|Al. (d) I-V-characteristics of a solar cell in the same configuration. 39

List of Tables

1	Overview of used materials, including supplier, purity and abbreviation.	18
2	Overview of used materials, including supplier, purity and abbreviation.	19
3	Spin coating parameters, used for preparation of thin films.	22
4	Overview of recipes for the preparation of MAPI films from lead acetate precursor solution.	23
5	Overview of recipes for the preparation of MAPI films from lead iodide precursor solution.	23
6	Overview of investigated passivation agents for MAPI thin films, including their abbreviation, chemical structure, active functional group, passivation target and reference from literature.	42

References

- [1] I. L. Braly, D. W. deQuilettes, L. M. Pazos-Outón, S. Burke, M. E. Ziffer, D. S. Ginger, H. W. Hillhouse, *Nature Photonics* **2018**, *12*, 355–361.
- [2] Y. Chen, L. Zhang, Y. Zhang, H. Gao, H. Yan, *RSC Advances* **2018**, *8*, 10489–10508.
- [3] D. W. deQuilettes, W. Zhang, V. M. Burlakov, D. J. Graham, T. Leijtens, A. Osherov, V. Bulović, H. J. Snaith, D. S. Ginger, S. D. Stranks, *Nature communications* **2016**, *7*, 1–9.
- [4] J. Lim, M. T. Hörantner, N. Sakai, J. M. Ball, S. Mahesh, N. K. Noel, Y.-H. Lin, J. B. Patel, D. P. McMeekin, M. B. Johnston, B. Wenger, H. J. Snaith, *Energy & Environmental Science* **2019**, *12*, 169–176.
- [5] C. M. Sutter-Fella, Y. Li, M. Amani, J. W. Ager, F. M. Toma, E. Yablonovitch, I. D. Sharp, A. Javey, *Nano letters* **2016**, *16*, 800–806.
- [6] H. Dong, S. Pang, Y. Zhang, D. Chen, W. Zhu, H. Xi, J. Chang, J. Zhang, C. Zhang, Y. Hao, *Nanomaterials (Basel Switzerland)* **2018**, *8*, 720.
- [7] I. Poli, S. Eslava, P. Cameron, *J. Mater. Chem. A* **2017**, *5*, 22325–22333.
- [8] B.-W. Park, N. Kedem, M. Kulbak, D. Y. Lee, W. S. Yang, N. J. Jeon, J. Seo, G. Kim, K. J. Kim, T. J. Shin, G. Hodes, D. Cahen, S. I. Seok, *Nature communications* **2018**, *9*, 1–9.
- [9] A. Upadhyaya, C. M. S. Negi, A. Yadav, S. K. Gupta, A. S. Verma, *Semiconductor Science and Technology* **2018**, *33*, 065012.
- [10] J. C. Yu, D. B. Kim, E. D. Jung, B. R. Lee, M. H. Song, *Nanoscale* **2016**, *8*, 7036–7042.
- [11] N. Wang, L. Cheng, R. Ge, S. Zhang, Y. Miao, W. Zou, C. Yi, Y. Sun, Y. Cao, R. Yang, Y. Wei, Q. Guo, Y. Ke, M. Yu, Y. Jin, Y. Liu, Q. Ding, D. Di, Le Yang, G. Xing, H. Tian, C. Jin, F. Gao, R. H. Friend, J. Wang, W. Huang, *Nature Photonics* **2016**, *10*, 699–704.
- [12] Z.-K. Tan, R. S. Moghaddam, M. L. Lai, P. Docampo, R. Higler, F. Deschler, M. Price, A. Sadhanala, L. M. Pazos, D. Credgington, F. Hanusch, T. Bein, H. J. Snaith, R. H. Friend, *Nature nanotechnology* **2014**, *9*, 687–692.
- [13] K. Lin, J. Xing, L. N. Quan, F. P. G. de Arquer, X. Gong, J. Lu, L. Xie, W. Zhao, Di Zhang, C. Yan, W. Li, X. Liu, Y. Lu, J. Kirman, E. H. Sargent, Q. Xiong, Z. Wei, *Nature* **2018**, *562*, 245–248.

- [14] J. Li, X. Shan, S. G. R. Bade, T. Geske, Q. Jiang, X. Yang, Z. Yu, *The journal of physical chemistry letters* **2016**, *7*, 4059–4066.
- [15] P. Würfel, U. Würfel, *Physics of Solar Cells: From Basic Principles to Advanced Concepts*, 3rd ed., Wiley-VCH, Weinheim, **2016**.
- [16] R. T. Ross, *The Journal of Chemical Physics* **1967**, *46*, 4590–4593.
- [17] Y. Chen, A. S. Yerramilli, L. Li, W. Qu, Y. Shen, Y. Song, T. L. Alford, *ACS Applied Energy Materials* **2018**, *1*, 2898–2906.
- [18] L. Yang, Y. Gao, Y. Wu, X. Xue, F. Wang, Y. Sui, Y. Sun, M. Wei, X. Liu, H. Liu, *ACS applied materials & interfaces* **2019**, *11*, 792–801.
- [19] K.-M. Lee, C.-J. Lin, B.-Y. Liou, S.-M. Yu, C.-C. Hsu, V. Suryanarayanan, *Organic Electronics* **2019**, *65*, 266–274.
- [20] M. Zhang, Z. Wang, B. Zhou, X. Jia, Q. Ma, N. Yuan, X. Zheng, J. Ding, W.-.-H. Zhang, *Solar RRL* **2018**, *2*, 1700213.
- [21] W. Zhang, Y. Li, X. Liu, D. Tang, X. Li, X. Yuan, *Chemical Engineering Journal* **2020**, *379*, 122298.
- [22] N. J. Jeon, J. H. Noh, Y. C. Kim, W. S. Yang, S. Ryu, S. I. Seok, *Nature materials* **2014**, *13*, 897–903.
- [23] Z. Guo, J. Zhuang, Z. Ma, H. Xia, J. Yi, W. Zhou, H. Lu, Y. Xiang, H. Li, *CrystEngComm* **2019**, *21*, 4753–4762.
- [24] M. Saliba, T. Matsui, J.-Y. Seo, K. Domanski, J.-P. Correa-Baena, M. K. Nazeeruddin, S. M. Zakeeruddin, W. Tress, A. Abate, A. Hagfeldt, M. Grätzel, *Energy & environmental science* **2016**, *9*, 1989–1997.
- [25] B. Hailegnaw, G. Adam, D. Wielend, J. D. Pedarnig, N. S. Sariciftci, M. C. Scharber, *The Journal of Physical Chemistry C* **2019**, *123*, 23807–23816.
- [26] H. Tang, S. He, C. Peng, *Nanoscale research letters* **2017**, *12*, 410.
- [27] Y. Yao, H. Yu, Y. Wu, Y. Lu, Z. Liu, X. Xu, B. Ma, Q. Zhang, S. Chen, W. Huang, *ACS omega* **2019**, *4*, 9150–9159.
- [28] K. Hąc-Wydro, P. Wydro, P. Dynarowicz-Łątka, *Thin Solid Films* **2008**, *516*, 8839–8843.
- [29] X. Zheng, Y. Hou, Bao, Chunxiong, J. Yin, F. Yuan, Z. Huang, K. Song, J. Liu, J. Troughton, N. Gasparini, C. Zhou, Y. Lin, D.-J. Xue, B. Chen, A. K. Johnston, N. Wei, M. N. Hedhili, M. Wei, A. Y. Alsalloum, P. Maity, B. Turedi, C. Yang, D. Baran, T. D. Anthopoulos, Y. Han, Z.-H. Lu, O. F. Mohammed, F. Gao, E. H. Sargent, O. M. Bakr, *Nature Energy* **2020**, *5*, 131–140.

- [30] B. Hailegnaw, V. Poscher, C. Ulbricht, H. Seelajaroen, I. Teasdale, Y. Salinas, N. S. Sariciftci, M. C. Scharber, *physica status solidi (a)* **2019**, *216*, 1900436.
- [31] X. Zhuang, Y. Zhang, J. Zhang, Y. Chen, Y. Zhu, *Materials Research Express* **2019**, *6*, 025512.
- [32] X. He, J. Wu, T. Wu, Z. Lan, M. Huang, *Energy Technology* **2019**, *7*, 346–351.
- [33] H. Miyamae, Y. Numahata, M. Nagata, *Chemistry Letters* **1980**, *9*, 663–664.
- [34] K. Lyczko, J. Narbutt, B. Paluchowska, J. K. Maurin, I. Persson, *Dalton transactions (Cambridge England : 2003)* **2006**, 3972–3976.
- [35] B. R. Nag, *Physics of Quantum Well Devices*, Kluwer Academic Publishers, Dordrecht, **2002**.
- [36] P. Würfel, *Journal of Physics C: Solid State Physics* **1982**, 3967–3985.
- [37] F. Herrmann, P. Würfel, *American Journal of Physics* **2005**, *73*, 717–721.
- [38] W. Shockley, H. J. Queisser, *Journal of Applied Physics* **1961**, *32*, 510–519.
- [39] B. Chen, P. N. Rudd, S. Yang, Y. Yuan, J. Huang, *Chemical Society reviews* **2019**, *48*, 3842–3867.
- [40] J. Bisquert, *The Physics of Solar Cells: Perovskites, Organics, and Photovoltaic Fundamentals*, CRC Press, Boca Raton, **2018**.
- [41] T. S. Sherkar, C. Momblona, L. Gil-Escrig, J. Ávila, M. Sessolo, H. J. Bolink, L. J. A. Koster, *ACS energy letters* **2017**, *2*, 1214–1222.
- [42] S. Zhang, S. M. Hosseini, R. Gunder, A. Petsiuk, P. Caprioglio, C. M. Wolff, S. Shoaee, P. Meredith, S. Schorr, T. Unold, P. L. Burn, D. Neher, M. Stolterfoht, *Advanced materials (Deerfield Beach Fla.)* **2019**, e1901090.
- [43] X. Zhang, J.-X. Shen, W. Wang, C. G. van de Walle, *ACS Energy Letters* **2018**, *3*, 2329–2334.
- [44] M. Grundmann, *The Physics of Semiconductors: An Introduction Including Devices and Nanophysics*, Springer-Verlag, Berlin Heidelberg, **2006**.
- [45] W. Shockley, W. T. Read, *Physical Review* **0005**, *1952*, 835–842.
- [46] H.-W. Chen, D. P. Gulo, Y.-C. Chao, H.-L. Liu, *Scientific reports* **2019**, *9*, 18253.
- [47] B. Hailegnaw, S. Paek, K. T. Cho, Y. Lee, F. Ongül, M. K. Nazeeruddin, M. C. Scharber, *Solar RRL* **2019**, 1900126.
- [48] N. S. Sariciftci, L. Smilowitz, A. J. Heeger, J. Wudl, *Science* **1992**, *285*, 1474–1476.

- [49] J. C. Hummelen, B. W. Knight, F. LePeq, F. Wudl, J. Yao, C. L. Wilkins, *Journal of Organic Chemistry* **1995**, *60*, 532–538.
- [50] S. Collavini, J. L. Delgado, *Sustainable Energy & Fuels* **2018**, *2*, 2480–2493.
- [51] Y. Shao, Z. Xiao, C. Bi, Y. Yuan, J. Huang, *Nature communications* **2014**, *5*, 5784.
- [52] Y. Lin, B. Chen, F. Zhao, X. Zheng, Y. Deng, Y. Shao, Y. Fang, Y. Bai, C. Wang, J. Huang, *Advanced materials (Deerfield Beach Fla.)* **2017**, *29*.
- [53] R. C. Haddon, *The Royal Society* **1993**, *343*, 52–62.
- [54] R. C. Haddon, *Science* **1993**, *261*, 1545–1550.
- [55] N. K. Noel, A. Abate, S. D. Stranks, E. S. Parrott, V. M. Burlakov, A. Goriely, H. J. Snaith, *ACS nano* **2014**, *8*, 9815–9821.
- [56] J. L. Cortina, Miralles, N., Sastre, A. M., M. Aguilar, *Hydrometallurgy* **1995**, *37*, 301–322.
- [57] K. Haç-Wydro, P. Wydro, P. Dynarowicz-Łątka, *Thin Solid Films* **2008**, *516*, 8839–8843.
- [58] Y. Yao, H. Yu, Y. Wu, Y. Lu, Z. Liu, X. Xu, B. Ma, Q. Zhang, S. Chen, W. Huang, *ACS omega* **2019**, *4*, 9150–9159.
- [59] H.-H. Fang, S. Adjokatse, H. Wei, J. Yang, G. R. Blake, J. Huang, J. Even, M. A. Loi, *Science Advances* **2016**, *2*, e1600534.
- [60] Y. Tian, M. Peter, E. Unger, M. Abdellah, K. Zheng, T. Pullerits, A. Yartsev, V. Sundström, I. G. Scheblykin, *Physical Chemistry Chemical Physics* **2015**, *17*, 24978–24987.
- [61] C. Bi, X. Zheng, B. Chen, H. Wei, J. Huang, *ACS Energy Letters* **2017**, *2*, 1400–1406.
- [62] M. Abdi-Jalebi, Z. Andaji-Garmaroudi, S. Cacovich, C. Stavrakas, B. Philippe, J. M. Richter, M. Alsari, E. P. Booker, E. M. Hutter, A. J. Pearson, S. Lilliu, T. J. Savenije, H. Rensmo, G. Divitini, C. Ducati, R. H. Friend, S. D. Stranks, *Nature* **2020**, *581*, E1.
- [63] M. Lu, J. Guo, P. Lu, L. Zhang, Y. Zhang, Q. Dai, Y. Hu, V. L. Colvin, W. W. Yu, *The Journal of Physical Chemistry C* **2019**, *123*, 22787–22792.
- [64] Z. Liu, D. Liu, H. Chen, L. Ji, H. Zheng, Y. Gu, F. Wang, Z. Chen, S. Li, *Nanoscale research letters* **2019**, *14*, 304.
- [65] Y. Fan, H. Qin, W. Ye, M. Liu, F. Huang, D. Zhong, *Thin Solid Films* **2018**, *667*, 40–47.

- [66] S. Tong, C. Gong, C. Zhang, G. Liu, D. Zhang, C. Zhou, J. Sun, S. Xiao, J. He, Y. Gao, J. Yang, *Applied Materials Today* **2019**, *15*, 389–397.
- [67] B.-G. Park, *Chemical Physics Letters* **2019**, *722*, 44–49.
- [68] D. S. Lee, J. S. Yun, J. Kim, A. M. Soufiani, S. Chen, Y. Cho, X. Deng, J. Seidel, S. Lim, S. Huang, A. W. Y. Ho-Baillie, *ACS Energy Letters* **2018**, *3*, 647–654.
- [69] H. Duim, H.-H. Fang, S. Adjokatse, G. H. ten Brink, M. A. L. Marques, B. J. Kooi, G. R. Blake, S. Botti, M. A. Loi, *Applied Physics Reviews* **2019**, *6*, 031401.
- [70] Z. Cheng, J. Lin, *CrystEngComm* **2010**, *12*, 2646.
- [71] Z. Xiao, R. A. Kerner, L. Zhao, N. L. Tran, K. M. Lee, T.-W. Koh, G. D. Scholes, B. P. Rand, *Nature Photonics* **2017**, *11*, 108–115.
- [72] Z. Xiao, R. A. Kerner, N. Tran, L. Zhao, G. D. Scholes, B. P. Rand, *Advanced Functional Materials* **2019**, *29*, 1807284.
- [73] V. L. Pool, A. Gold-Parker, M. D. McGehee, M. F. Toney, *Chemistry of Materials* **2015**, *27*, 7240–7243.
- [74] J. I. Uribe, J. Ciro, J. F. Montoya, J. Osorio, F. Jaramillo, *ACS Applied Energy Materials* **2018**, *1*, 1047–1052.
- [75] Q. Chen, H. Zhou, Y. Fang, A. Z. Stieg, T.-B. Song, H.-H. Wang, X. Xu, Y. Liu, S. Lu, J. You, P. Sun, J. McKay, M. S. Goorsky, Y. Yang, *Nature communications* **2015**, *6*, 7269.
- [76] M. M. Tavakoli, P. Yadav, D. Prochowicz, M. Sponseller, A. Osherov, V. Bulović, J. Kong, *Advanced Energy Materials* **2019**, *9*, 1803587.
- [77] Q. Li, Y. Zhao, R. Fu, W. Zhou, Y. Zhao, X. Liu, D. Yu, Q. Zhao, *Advanced materials (Deerfield Beach Fla.)* **2018**, e1803095.
- [78] N. Yantara, F. Yanan, C. Shi, H. A. Dewi, P. P. Boix, S. G. Mhaisalkar, N. Mathews, *Chemistry of Materials* **2015**, *27*, 2309–2314.
- [79] Y. Luo, S. Gamliel, S. Nijem, S. Aharon, M. Holt, B. Stripe, V. Rose, M. I. Bertoni, L. Etgar, D. P. Fenning, *Chemistry of Materials* **2016**, *28*, 6536–6543.
- [80] D.-Y. Son, J.-W. Lee, Y. J. Choi, I.-H. Jang, S. Lee, P. J. Yoo, H. Shin, N. Ahn, M. Choi, D. Kim, N.-G. Park, *Nature Energy* **2016**, *1*.
- [81] X. Li, C.-C. Chen, M. Cai, X. Hua, F. Xie, X. Liu, J. Hua, Y.-T. Long, H. Tian, L. Han, *Advanced Energy Materials* **2018**, *8*, 1800715.
- [82] S. Yang, J. Dai, Z. Yu, Y. Shao, Y. Zhou, X. Xiao, X. C. Zeng, J. Huang, *Journal of the American Chemical Society* **2019**, *141*, 5781–5787.

- [83] S. Yang, W. Liu, L. Zuo, X. Zhang, T. Ye, J. Chen, C.-Z. Li, G. Wu, H. Chen, *Journal of Materials Chemistry A* **2016**, 4, 9430–9436.
- [84] Q. Li, *Nanomaterials for Sustainable Energy*, Springer International Publishing, Cham, **2016**.
- [85] A. G. Aberle, R. Hezel, *Progress in Photovoltaics: Research and Applications* **1997**, 5, 29–50.
- [86] R. S. Bonilla, B. Hoex, P. Hamer, P. R. Wilshaw, *physica status solidi (a)* **2017**, 214, 1700293.
- [87] B. Hoex, J. Schmidt, P. Pohl, M. C. M. van de Sanden, W. M. M. Kessels, *Journal of Applied Physics* **2008**, 104, 044903.
- [88] J. R. Elmiger, R. Schieck, M. Kunst, *Journal of Vacuum Science & Technology A: Vacuum Surfaces and Films* **1997**, 15, 2418–2425.
- [89] W. L. Warren, F. C. Rong, E. H. Poindexter, G. J. Gerardi, J. Kanicki, *Journal of Applied Physics* **1991**, 70, 346–354.
- [90] Q. Ou, X. Bao, Y. Zhang, H. Shao, G. Xing, X. Li, L. Shao, Q. Bao, *Nano Materials Science* **2019**, 1, 268–287.
- [91] A. Al-Ahmadi, *State-of-the-Art of Quantum Dot System Fabrications*, InTech, Rijeka, Croatia, **2012**.
- [92] W. Huang, T. Bu, F. Huang, Y.-B. Cheng, *Joule* **2020**, 4, 975–979.
- [93] G. Rose, *Annalen der Physik* **1839**, 124, 558–561.
- [94] V. M. Goldschmidt, **1926**, 21, 477–485.
- [95] *Rational design of solar cells for efficient solar energy conversion*, First edition, (Eds.: A. Pandikumar, R. Ramaraj), John Wiley & Sons, Hoboken NJ, **2018**.
- [96] E. M. Hutter, M. C. Gélvez-Rueda, A. Osherov, V. Bulović, F. C. Grozema, S. D. Stranks, T. J. Savenije, *Nature materials* **2017**, 16, 115–120.
- [97] J. Lin, H. Chen, Y. Gao, Y. Cai, J. Jin, A. S. Etman, J. Kang, T. Lei, Z. Lin, M. C. Folgueras, L. N. Quan, Q. Kong, M. Sherburne, M. Asta, J. Sun, M. F. Toney, J. Wu, P. Yang, *Proceedings of the National Academy of Sciences of the United States of America* **2019**, 116, 23404–23409.
- [98] X. Lü, W. Yang, Q. Jia, H. Xu, *Chemical science* **2017**, 8, 6764–6776.
- [99] C. Zhang, D. Sun, C.-X. Sheng, Y. X. Zhai, K. Mielczarek, A. Zakhidov, Z. V. Vardeny, *Nature Physics* **2015**, 11, 427–434.
- [100] A. N. Corpus-Mendoza, P. M. Moreno-Romero, H. Hu, *AIP Advances* **2018**, 8, 055221.

- [101] D. Ji, M. Na, S. Wang, H. Zhang, K. Zhu, C. Zhang, X. Li, *Scientific reports* **2018**, *8*, 12492.
- [102] A. Mattoni, C. Caddeo, *The Journal of Chemical Physics* **2020**, *152*, 104705.
- [103] G. Kieslich, S. Sun, A. K. Cheetham, *Chemical science* **2015**, *6*, 3430–3433.
- [104] J. Caram, N. Budini, R. D. Arce, *Matéria (Rio de Janeiro)* **2018**, *23*, 791.
- [105] A. Kojima, K. Teshima, Y. Shirai, T. Miyasaka, *Journal of the American Chemical Society* **2009**, *131*, 6050–6051.
- [106] Best Research-Cell Efficiencies, nrel.gov/pv/cell-efficiency, **26.04.2020**.
- [107] F. Jonas, L. Schrader, *Synthetic Metals* **1991**, *41*, 831–836.
- [108] X. Fan, W. Nie, H. Tsai, N. Wang, H. Huang, Y. Cheng, R. Wen, L. Ma, F. Yan, Y. Xia, *Advanced science (Weinheim Baden-Wurttemberg Germany)* **2019**, *6*, 1900813.
- [109] G. Adam, M. Kaltenbrunner, E. D. Glowacki, D. H. Apaydin, M. S. White, H. Heilbrunner, S. Tombe, P. Stadler, B. Ernecker, C. W. Klampfl, N. S. Sariciftci, M. C. Scharber, *Solar Energy Materials and Solar Cells* **2016**, *157*, 318–325.
- [110] C. L. Watts, L. Aspitarte, Y.-H. Lin, W. Li, R. Elzein, R. Addou, M. J. Hong, G. S. Herman, H. J. Snaith, J. G. Labram, *Communications Physics* **2020**, *3*.
- [111] R. Wang, M. Mujahid, Y. Duan, Z.-.-K. Wang, J. Xue, Y. Yang, *Advanced Functional Materials* **2019**, *29*, 1808843.
- [112] F. Palazon, D. Pérez-del-Rey, S. Marras, M. Prato, M. Sessolo, H. J. Bolink, L. Manna, *ACS Energy Letters* **2018**, *3*, 835–839.
- [113] A. Krishna, M. A. Akhavan Kazemi, M. Sliwa, G. N. M. Reddy, L. Delevoye, O. Lafon, A. Felten, M. T. Do, S. Gottis, F. Sauvage, *Advanced Functional Materials* **2020**, *30*, 1909737.



KATARINA GUGUJONOVIĆ

WORK EXPERIENCE

- 2012 Belan Ziviltechniker GmbH, Internship (8 weeks)
- 2013 – 2015 Takeda Austria, Chemical Laboratory Technician
Pharmaceutical Production (Actovegin)
Wet Chemistry Analysis for Quality Control
- 2015 – 2016 Cioccolateria Marinello, Sales Advisor
- 2016, 2017 Tannpapier GmbH, Internship (7 weeks)
- 2018 Linz Institute of Organic Solar Cells, Internship (3 month)
- 2016 – present Rag GmbH, Sales Advisor

EDUCATION

- 2008 – 2013 Höhere Technische Bundeslehranstalt für Chemische Betriebstechnik, Wels
(College of Chemical Engineering Specialising in Chemical Industrial Engineering, Wels)
- 2015 – 2019 Johannes Kepler University, Linz
Bachelor's Program: Technische Chemie (Chemical Technology)
- 2019 – present Johannes Kepler University, Linz
Master's Program: Chemistry and Chemical Technology with focus on: Physical Chemistry, Analytical Chemistry and Inorganic Chemistry

MASTER'S THESIS

Photoluminescence Enhancement in Perovskite Thin Films

BACHELOR'S THESIS

An Alternative Non-fullerene Acceptor for Organic Solar Cells

DIPLOMARBEIT (COLLEGE PROJECT)

Synthese und Syntheseoptimierung N-substituierter Melamine
(Synthesis and Synthesis Optimization of N-substituted Melamines)

PERSONAL DATA

*19.07.1994 in Wels

Excellent German and English Skills

Serbian Native Speaker

Hobby Photographer

CONTACT

Johann-Wilhelm-Klein Straße 70/ 1201

4040 Linz

0660 5014457

k.gug@live.de